Pentagonal and Hexagonal Macrorings of Porphyrin Dimers Exhibiting Light-Harvesting Antenna Function

Academic Dissertation

by

Fatin Hajjaj

Division of Supramolecular Science. Graduate School of Materials Science. Nara Institute of Science and Technology (**NAIST**).

Pentagonal and Hexagonal Macrorings of Porphyrin Dimers Exhibiting Light-Harvesting Antenna Function

by

Fatin Hajjaj

A dissertation submitted to Nara Institute of Science and Technology in partial fulfillment of the requirements for the degree

DOCTOR OF ENGINEERING

Approved, Dissertation Committee:

Prof. Yoshiaki Kobuke, Chair

Division of Supramolecular Science

Prof. Mikio Kataoka

Division of Bioenergetics & Biophysics

Prof. Kiyomi Kakiuchi

Division of Synthetic Organic Chemistry

Prof. Masaki Aihara

Division of Theoretical Condensed Matter Physics

Nara, Japan

September, 2006

Contents

Chapter 1 Introduction

1.1- Bacterial light-harvesting system

The foremost biological process which builds on fundamental supramolecular and physical concepts is the process of photosynthesis which sustains all life on earth. Photosynthesis is carried out by many different organisms, i.e., plants, algae and photosynthetic bacteria which all have developed highly efficient and optimized systems to collect the light of the sun and to use the light energy as the driving force for their metabolic reactions.

Bacterial photosynthetic antenna complexes employ large numbers of porphyrinic pigments bound to proteins (e.g., chlorophylls, bacteriochlorophylls) to capture a large cross section of dilute sunlight and funnel energy to the reaction centers. In the reaction center (RC) the harvested energy is converted into a stable transmembrane charge separation through a sequence of electron-transfer reactions.[1] Time-resolved picosecond measurements showed that this conversion process is typically finished within ~100 ps, explaining the high overall quantum yield (95%) of the process.[2]

A major breakthrough in our understanding of the organization of the bacterial light-harvesting antenna and consequently of the photosynthesis process itself came

with the discovery of the structure of the LH2 complex of *Rps. acidophila* by Cogdell and co-workers in 1995,[3a] followed by the structure of *Rs. molischianum* by Michel and Schulten and co-workers in 1996.[3b] In these photosynthetic bacteria, the antenna complexes (LH1, LH2 and LH3) are deliberately organized in symmetric structures that assume the shape of a ring to achieve an efficient energy migration among hundreds of pigments through excitation energy hopping (EEH) process without non-energy transfer quenching. The peripheral antenna (LH2) forms two macrocyclic structures: B800 with 9 bacteriochlorophyll *a* (Bchl *a*) molecules and B850 with 18 Bchl *a* molecules.[3a, b] The structural complexity in the circular arrangement of 18 Bchls *a* is that they are not evenly distributed. They are composed of 9 Bchl *a* dimeric forms with Mg-Mg intradimer distance of 8.7 Å, whereas it is 9.7 Å between the adjacent dimeric units. These dimer units are strongly coupled to form exciton states, as a consequence of the close slipped-cofacial arrangement which is maintained by the coordination from imidazolyl residue to Mg center. The remaining 9 Bchl *a* in B800 are located just beneath the 18 Bchl *a* macroring by forming a perpendicular ring. The Mg-Mg distance between B800 Bchls *a* is 21 Å, that is, Bchls *a* may be regarded as monomers and thus are only weakly interacting. These spatial arrangements provide a most efficient energy transfer via Förster induced dipole-dipole resonance from the short- to the

long-wavelength-absorbing pigments within the photosynthetic unit. On the basis of a low-resolution electron density map and the analogy between LH1 and LH2, it is now generally believed that LH1 is a 16-fold symmetric ring composed of 32 Bchls with the RC in its center.[3c] Since the core antenna (LH1) absorbs at longer wavelengths (870 -1000 nm), the light-harvesting system functions as an energy funnel towards the RC. This transfer of energy form LH2 to LH1 and subsequently to the RC occurs in vivo on a timescale of 5 to 50 ps,[2b] very fast compared to the excited state decay of isolated LH2 complexes, which corresponds to a lifetime of about 1 ns (Figure 1.1).

The photosynthetic macrorings in purple bacteria are believed to be associated with the most important function in light harvesting and thus stimulated a large body of experimental and theoretical work on photosynthesis.

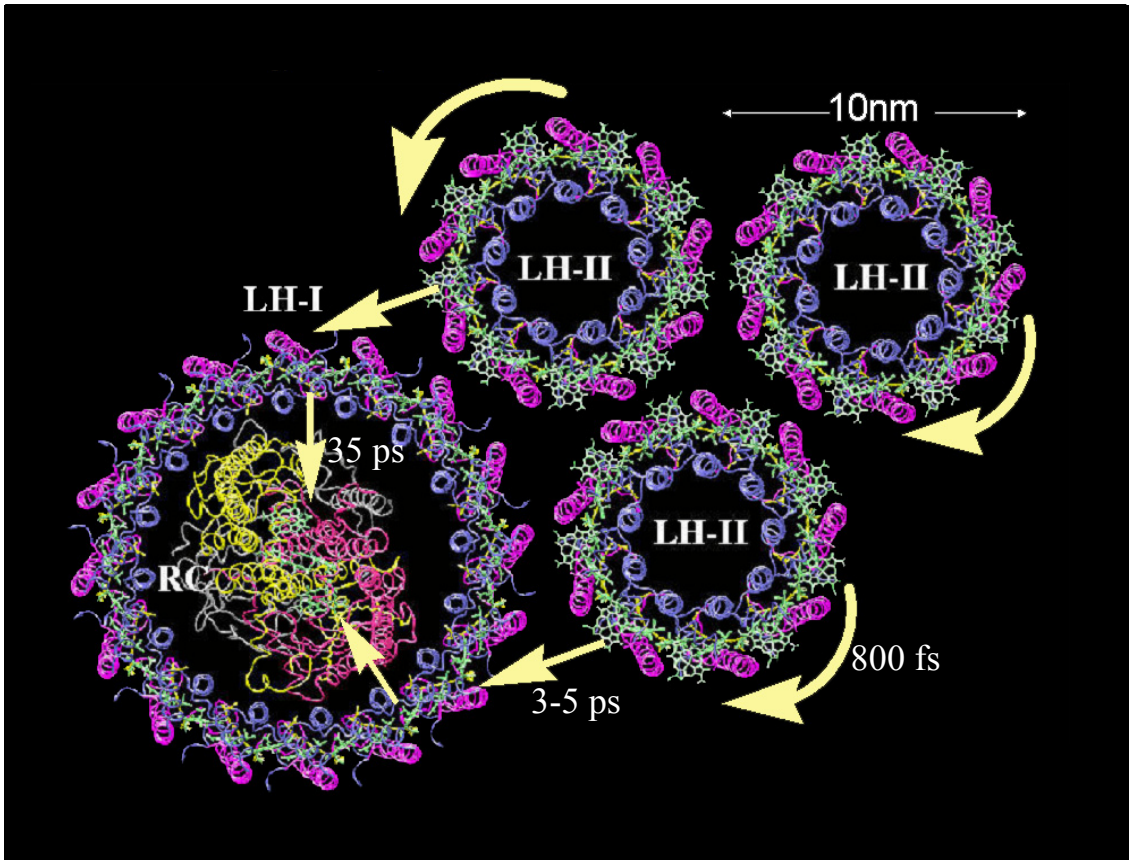

Figure 1.1. Model for the photosynthetic unit (PSU) of the purple bacterium *Rb. sphaeroides*. The PSU consists of two types of protein-pigment complexes: the photosynthetic reaction center (RC) and the light-harvesting complexes (LH). The arrows represent excitation energy which is efficiently transferred through ring-arranged porphyrins (LHs) to a distant reaction center for the photo-induced redox processes. While LH1 is tightly bound to the RC, LH2 is not directly associated with it, but transfers energy to the RC via LH1. Figure reproduced from Ref. 3 (d).

1.2- Artificial light-harvesting systems

1.2.1- Trends in constructing photosynthetic antenna mimics. A major objective of artificial photosynthesis is to design and construct synthetic architectures that rival the natural systems in light absorption and excited-state energy transfer properties. Mimicking the natural photosynthetic process requires synthetic models of all the crucial components and linking them together into a working molecular assembly that exhibits antenna function. The antenna effect can only be obtained in molecular assemblies suitably organized in space and energy domains. Each molecular component must absorb the incident light, and the excited state obtained this way must transfer electronic energy to the nearby component before undergoing radiative or nonradiative deactivation.

Owing to their synthetic accessibility, rigid and planar geometry as well as their electronic properties and their ability to complex almost any kind of metal ions, porphyrins are one of the potential candidates for light-harvesting antennae, synthetic analogues of the natural light-harvesting chromophores.[4] Synthetic porphyrin-based light-harvesting arrays are essential for probing the effects of molecular organization on energy migration processes. A general feature of many synthetic approaches is the use of covalent linkers to join porphyrinic pigments in an array, thereby fixing the distance

of separation between the pigments.[4c, 5] In addition to its mechanical role, the linker can provide a conduit that enables through-bond electronic communication between chromophores for energy transfer. In this respect, the linker provides a feature that has no counterpart in the natural systems, where the pigments are assembled via noncovalent interactions. The overall structures of the covalently linked porphyrin arrays, however, are still remote from those of natural light-harvesting systems, mainly due to a lack of fine control of the synthetic capabilities which require elaborate and time consuming work. Supramolecular assembly by hydrogen bonding and metal-to-ligand coordination is another promising approach to achieve the construction of artificial antenna models. This approach has yielded light-harvesting arrays with enhanced efficiency in light-harvesting and electronic communication.[6] In this way, it becomes possible to prepare stable self-assembled macrocyclic arrays from large numbers of porphyrins as mimics of light-harvesting complexes in photosynthetic bacteria.

1.2.2- Kobuke's approach and previous work. Self-assembling into macrocyclic porphyrin arrays through non-covalent bonds is challenging from a viewpoint of synthetic accessibility to nature's methodology.[7,8] In an attempt to develop artificial photosynthetic systems, Kobuke *et al*. have sought to construct LH complexes with the maximum use of intermolecular interactions without any peptide matrixes. A method of obtaining extremely stable LH macrocycles has been established by employing imidazolylporphyrinatozinc(II) dimer as the building block.[8a,f] This molecular design should provide important characteristics for constructing macrocyclic LH antenna model. First, the complementary coordination between imidazolyl and central zinc ion is further facilitated by π-π stacking interactions between porphyrins and characterized by a large association constant ($Ka \sim 10^{11}\ M^{-1}$) in noncoordinating solvents. The resulting supramolecule show a large splitting of Soret band (~1300 cm^{-1}) through exciton coupling interaction of two porphyrins in a slipped-cofacial arrangement in close distance. This split Soret band, along with upfield shifts in the resonances of the coordinating imidazolyl protons from the two porphyrins in the ^1H NMR spectrum, are highly characteristic of self-complementary dimer formation. It is noteworthy that the interplanar distance between the two porphyrins is close to 3.2 Å, and the Zn-to-Zn distance is 6.13 Å, making the slipped-cofacial structure very similar to those of the

natural LH complexes.[9a] The second important point for any LH mimic designed to replicate the photosynthetic model is that the central metal ion should not quench the singlet excitation energy. Most transition metal ions quench the fluorescence, and the metalloporphyrins may be regarded as dyestuffs rather than photosynthetic models. Cyclic dodecamers formed through axial coordination of substituted pyridines to six-coordinated cobalt porphyrins have been demonstrated.[7b] Although the resultant macroring structurally resembles natural LH2, no LH function is expected from non-fluorescent cobalt porphyrins. Mg and Zn ions are useful candidates from among the other metal ions that might be inserted into the center of porphyrin macrocycles. Photosynthetic systems certainly employ Mg ions. However, extensive studies focusing on the Zn complexes of porphyrins have been undertaken, since Zn(II), having a d^{10} structure, can be a good substitute for Mg(II). Although the fluorescence quantum yields of Zn(II) porphyrins are inferior to those of Mg(II) porphyrins, the former have obvious advantages such as permitting easy introduction of the metal into the structure, stability in acidic conditions, and durability when exposed to oxidation conditions. In fact, organisms living under conditions of extreme heat and acidity near sea volcanoes have been found to employ Zn substitutes.[9b] Furthermore, zinc porphyrin has an additional merit from the viewpoint of coordination chemistry. Since Zn(II) can accept

only one axial coordination, the dimer is the only coordination product without any additional complexation events.

The use of an appropriate linker is another important factor affecting the formation of LH macrocycles. In order to arrange the complementary coordination units into a ring structure, two imidazolyl zinc porphyrins were connected through a *m*-phenylene spacer to fix the angle at 120°, affording the so-called "gable porphyrin". In contrast to the *meso*-*meso*-coupled bis(imidazolyl)porphyrinatozinc(II), which grows linearly into a giant array, [6b] the spatial orientation of gable porphyin is expected to give a close ring under appropriate conditions (Figure 1.2).

In general it is difficult to assemble donor molecules in a highly condensed state because of formation of undesired energy dissipation processes, e.g., concentration quenching, aggregation quenching, and nondirectional energy transfer, in homogenous solution. However, the arrangement of chromophores in Kobuke's macroring systems did not show any sign of fluorescence quenching and served as a platform to enable excitation energy hopping (EEH) processes along the ring.[10] Taken together, these LH macrorings have proven to be relevant and good antenna models for artificial photosynthesis.

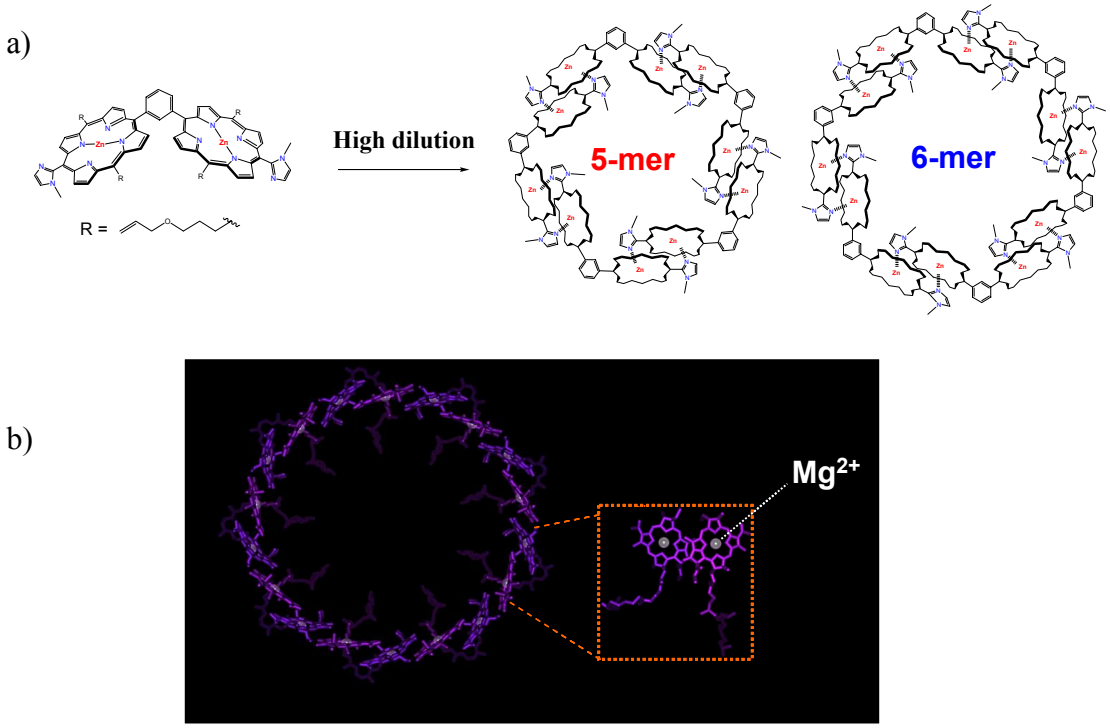

Figure 1.2. (a) A schematic diagram showing the formation of macrorings by the spontaneous assembly of zinc gable porphyrins into slipped-cofacial dimers. The hexameric macroring is the first example of porphyrin macroring composed of dimer units that has distances and orientations of zinc porphyrin units in close analogy to the natural LH2-B850. (b) The LH2-B850 complex of *Rps. acidophila* is arranged in macroring structure with use of nine bacteriochlorophyll-*a* dimers, which are characterized as being in slipped-cofacial orientations to each other. The cyclic structure is maintained by intermolecular forces, especially the coordination of imidazolyl residues to Mg centers. Figure 1.2 (b) reproduced from the website of Prof. R. Cogdell.

1.2.3- This work: supramolecular macrorings of 1,3- bis(ethynyl)phenylene-linked bis(imidazolylporphyrin) as a light-harvesting antenna mimic. As a continuing effort to construct efficient LH antenna models for artificial photosynthesis, we have explored the supramolecular formation of a larger macroring from bis(zinc-imidazolylporphyrin) linked by a *m*-bis(ethynyl)phenylene spacer (Figure 1.3).[8d] In order to ensure that the new molecular design favors the formation of an antenna ring, the basic characteristics designed into the chromophores of the previous *m*-phenylene-linked macrorings were preserved.[8a,e,f] However, in the latter rings, the steric crowding from the interaction of the phenyl *ortho* protons with the porphyrin β-hydrogens results in an orthogonal configuration of porphyrin and phenylene planes, thereby limiting the electronic communications. In this work, we have sought to remove the steric barrier between the aromatic systems and this has been accomplished through an intervening acetylene moiety between the phenyl and porphyrin rings. Introduction of the ethyne moiety between porphyrin and phenylene allows free rotation along the ethyne axis, and an intimate electronic communication among porphyrins would occur as a result of the coplanar conformation. Owing to their synthetic versatility and fascinating optical properties, phenylethynyl linkers have been employed extensively to construct porphyrin cyclic arrays with the goal of optimizing photophysical properties.[11]

With this in mind, the synthesis of new macrocyclic porphyrin arrays has been carried out in the present work by means of the complementary coordination of *m*-bis(ethynylene)phenylene-linked imidazolylporphyrinatozinc(II). The superiority of the *m*-bis(ethynylene)phenylene-linked macrorings over the *m*-phenylene-linked ones in terms of synthetic accessibility, molecular detection (NMR and STM) and antenna function will be discussed and compared in the proceeding chapters.

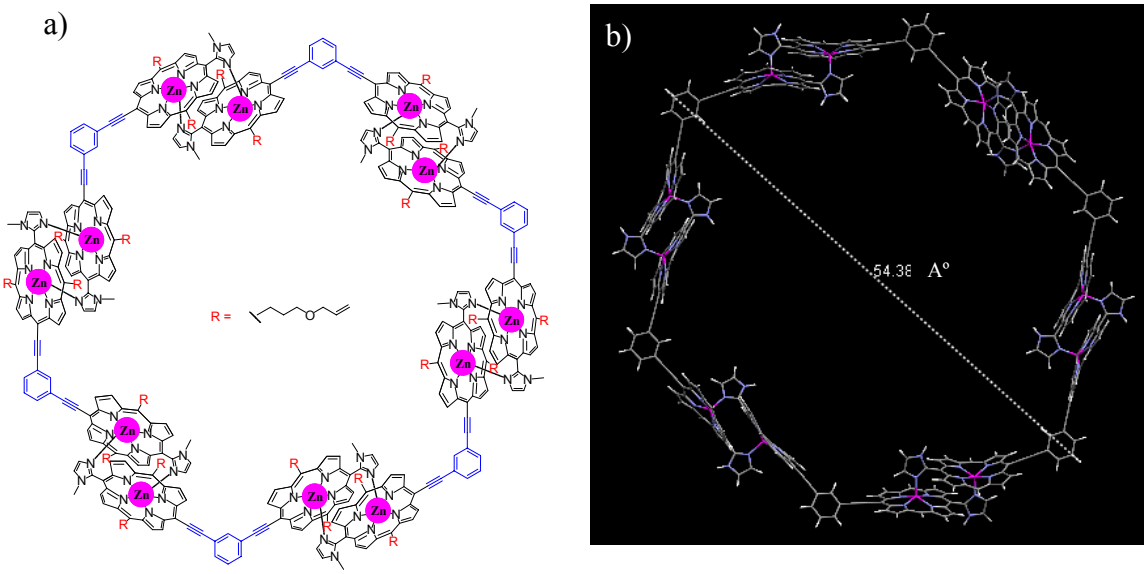

Figure 1.3. (a) The anticipated macrocyclic structure by the supramolecular assembly of zinc *m*-bisethynl gable porphyrin. (b) Molecular model represents the energy-minimized structure of the macroring in (a). The molecular model was created in universal force field. The substituents at the porphyrin *meso*-position were replaced by hydrogen atoms for visual clarity.

Chapters 2-4 Results and Discussion

Chapter 2- Synthesis and Purification of Macrorings and Reference Porphyrins

2.1- Preparation of gable porphyrin. A new approach has been established to construct macrorings composed of porphyrin dimer units that exploits sequential Pd-mediated cross-coupling reactions[12] and the self assembly of bis(zinc-imidazolylporphyrin) linked by a *m*-bis(ethynyl)phenylene spacer (**Zn-EP-Zn**). The desired macrorings require **Zn-EP-Zn** building block which can be obtained by the metalation of an appropriate gable porphyrin (**H_2-EP-H_2** or **H_2-EP-Zn**). We first attempted to prepare precursor **H_2-EP-H_2** as depicted in Scheme 1. Following a reported method,[13] **H_2-1** was prepared by the condensation of *N*-methylimidazolealdehyde[8e] **1** (2 equiv), 1-trimethylsilylethynylaldehyde[13] **2** (1 equiv) and *meso*-(4-allyloxybutyl)dipyrromethane[8e] **3** (2 equiv) in the presence of trifluoroacetic acid (TFA, 3 equiv) followed by oxidation with 2,3-dichloro-5,6-dicyano-1,4-benzoquinone (DDQ, 1.5 equiv) which gave **H_2-1** in 10% yield. Cleavage of the trimethylsilyl group (TMS) by *n*-tetrabutylammonium fluoride (TBAF) afforded **H_2-2** in 98% yield. When porphyrin **H_2-2** (2 equiv) and 1,3-diiodo-benzene (1 equiv) were reacted in the presence of the catalyst $Pd_2dba_3/AsPh_3$, the desired **H_2-EP-H_2** was obtained along with **4**. Oxidative coupling product **4**

generally accompanies the palladium catalyzed coupling reaction of ethynylporphyrins. Unfortunately, **H_2-EP-H_2** could not be separated from **4** effectively by various chromatographical techniques (SiO_2, Al_2O_3, and gel permeation chromatography (GPC)) owing to the similarity of polarities and molecular volumes.

Scheme 1. Synthesis of **H_2-EP-H_2** bisporphyrin

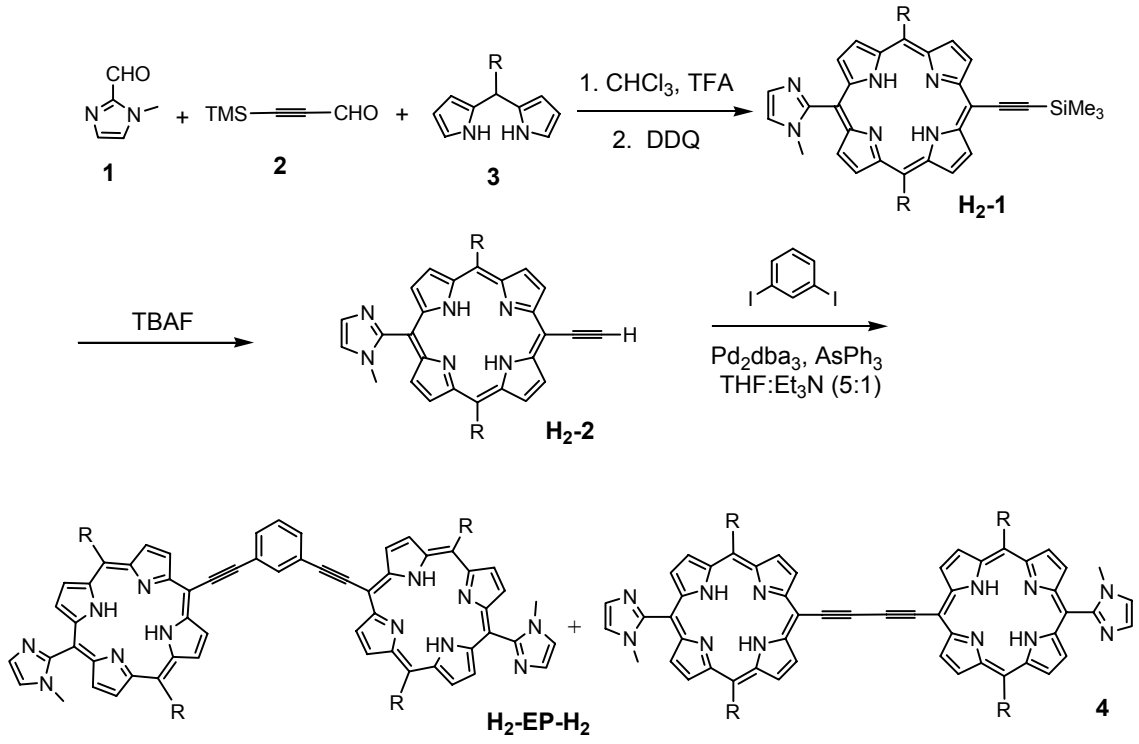

Thus, we gave up the synthesis of **H_2-EP-H_2** and opted for the approach in Scheme 2. First, porphyrin bearing one iodophenyl ethynyl group (**H_2-3**) was prepared in 78% yield from **H_2-2** with an excess 1,3-diiodo-benzene in the presence of the catalyst $Pd_2dba_3/AsPh_3$.

Scheme 2. Synthesis of **H_2-EP-Zn** bisporphyrin

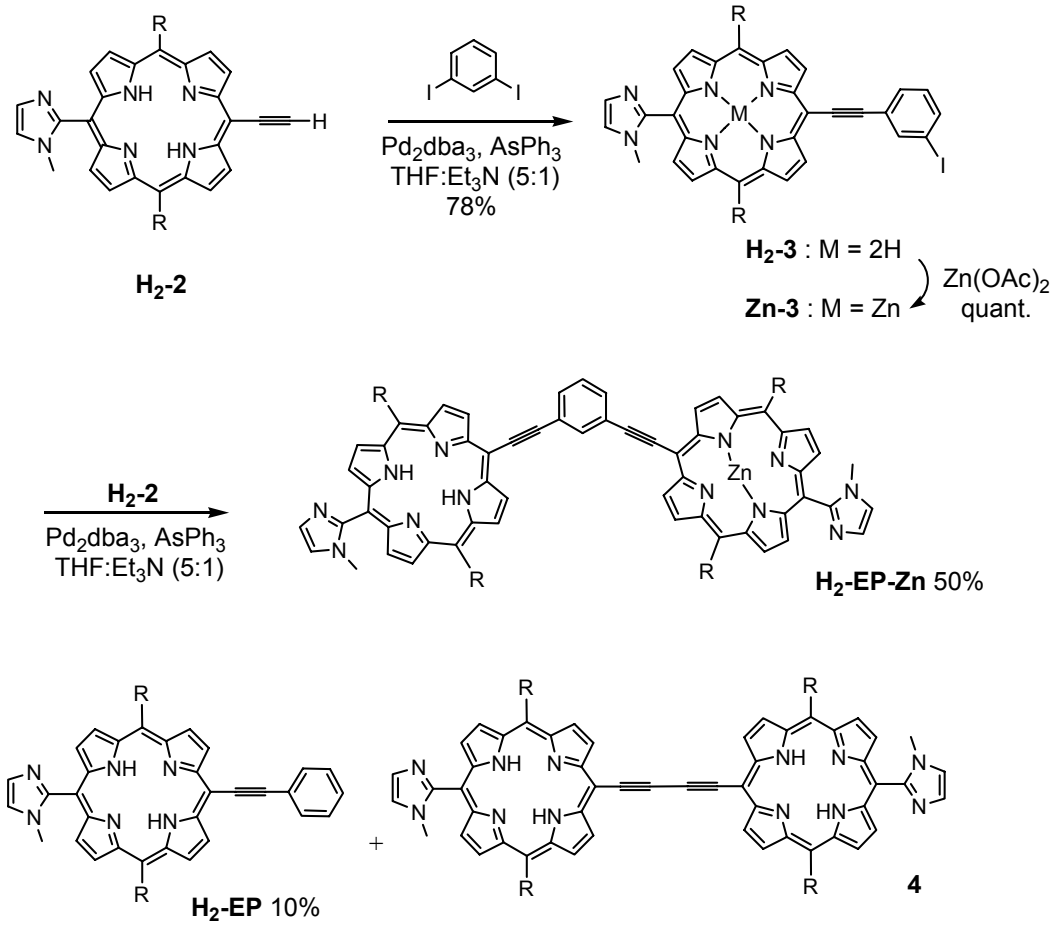

R = $(CH_2)_3OCH_2CH{=}CH_2$

Treatment of a chloroform solution of **H_2-3** (2.0 mM) with a methanol solution of zinc(II) acetate afforded **Zn-3** in a quantitative yield. The latter was cross-coupled with **H_2-2** in the presence of Pd(0) to provide **H_2-EP-Zn** as the dominant product along with **H_2-EP** and **4**. This time, **H_2-EP-Zn** was isolated successfully in 50% yield by gel permeation chromatography with pyridine as an eluent. In this coupling reaction, using a catalytic amount of Pd_2dba_3 (0.16 equiv) in diluted reaction mixture (~1.0 mM) at

room temperature was required to control the formation of **4** and **H_2-EP.** The latter was isolated in 10% yield, and its zinc complex **Zn-EP** was exploited for the synthesis of benchmark porphyrins for comparison purposes in the photophysical investigation.

Based on the previous result,[8a,e,f] the synthetic advantage of employing stepwise Sonogashira-coupling reactions in the introduction of diethynylbenzene linker is that the key building block for the macroring (**H_2-EP-Zn**) was afforded in higher yield relative to the previous approach which gave gable porphyrin (the building block of *m*-phenylene-linked macrorings) in ~17% yield. [8e]

2.2- Construction of macrorings: zinc(II) insertion into gable porphyrin and the reorganization process. An acetate method was adopted to insert zinc(II) ion into gable porphyrin under mild condition at room temperature. Zinc insertion converted the mono zinc porphyrin, **H_2-EP-Zn**, to the corresponding zinc complex **Zn-EP-Zn** which was spontaneously organized into oligomers by the complementary coordination of imidazolyl residues to Zn centers (Scheme 3).[8] GPC analysis of **Zn-EP-Zn** showed a broad molecular weight distribution with sharp spikes at longer retention times, which suggests the formation of oligomers of smaller molecular weights (Figure 2.1, red curve). The pattern of the first chromatogram was close to those obtained in the cases of *m*-phenylene-linked macrorings,[8a,f] suggesting that the formation of specific cyclic

oligomers was accompanied by the formation of a significant amount of linear oligomers.

Scheme 3. Metalation of **H_2-EP-Zn** and the reorganization of **Zn-EP-Zn** into rings

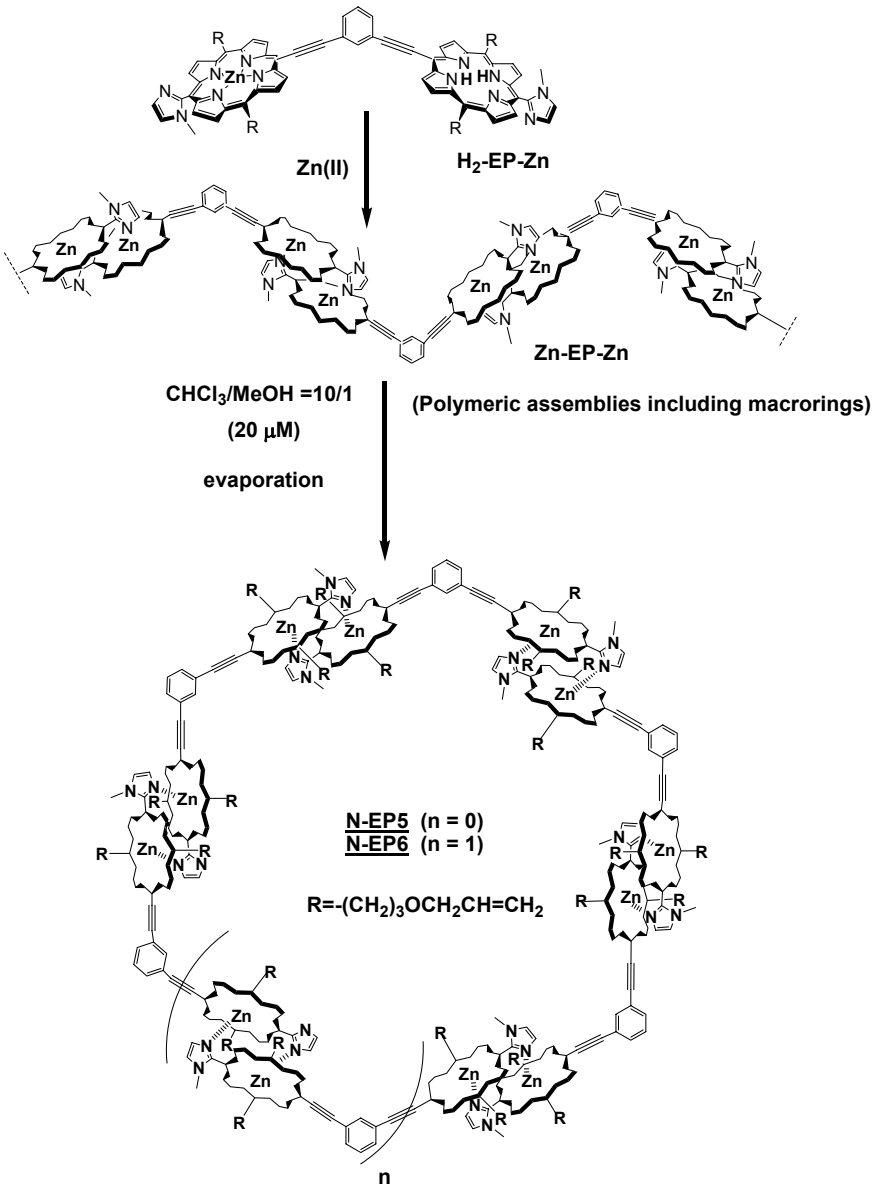

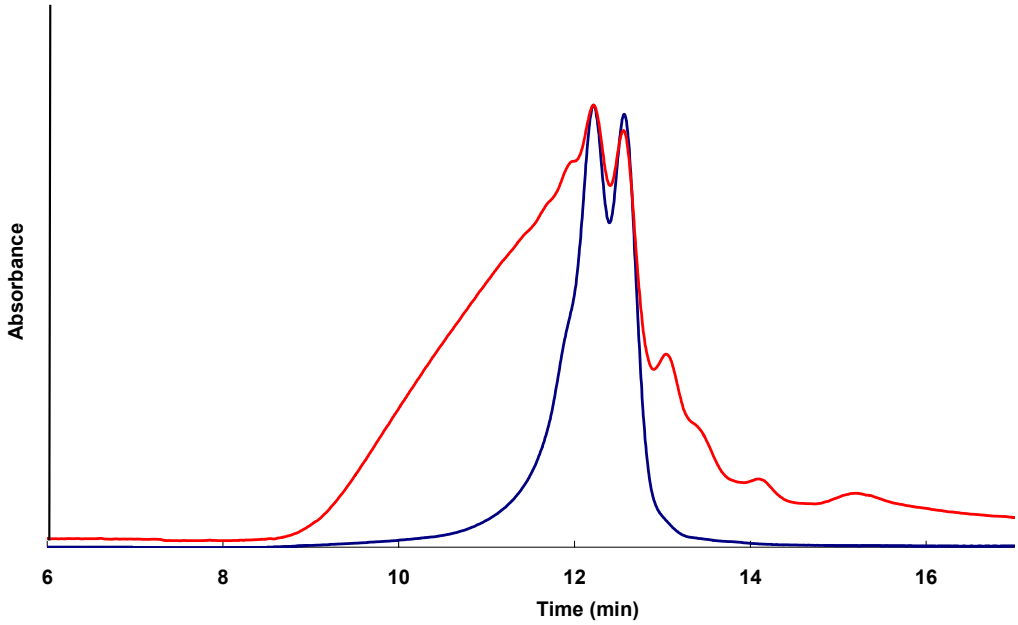

Figure 2.1. GPC chromatograms of **Zn-EP-Zn** before (red curve) and after (blue curve) the reorganization. Column: JAIGEL-3HA. Eluent: $CHCl_3$ with a flow rate = 1.2 ml/ min. Monitored at 420 nm.

In a previous communication,[8a] a reorganization procedure had been established to convert the once formed structure into macrocyclic arrays and this reorganization principle was applied to **Zn-EP-Zn** assembly. To dominate the intramolecular cyclization, **Zn-EP-Zn** assembly was dissociated to smaller oligomers by dissolving in 20.0 μM of $CHCl_3$/MeOH = 10/1 (v/v) and allowed to stand at room temperature for 1 day. During this period, conversion into ring complexes proceeded in good yield. The solvents were then evaporated at 26°C under reduced pressure as quickly as possible. The evaporation process must be controlled carefully. During the concentration process, the solvent becomes methanol-rich, and the coordinated dimer tends to dissociate.

The cyclic assemblies dissociated are transformed into polymeric assemblies at higher concentrations.[8a,f,14] Evaporation under these circumstances increases the amount of oligomer, and thus, must be performed quickly. The use of large volumes (more than 500 ml) should be avoided for a reason. Analytical GPC trace of **Zn-EP-Zn** after the reorganization (Figure 2.1, blue curve) showed two converged peaks, putative cyclic hexamer and pentamer **N-EP6** and **N-EP5**, respectively, and the higher molecular weight components disappeared.

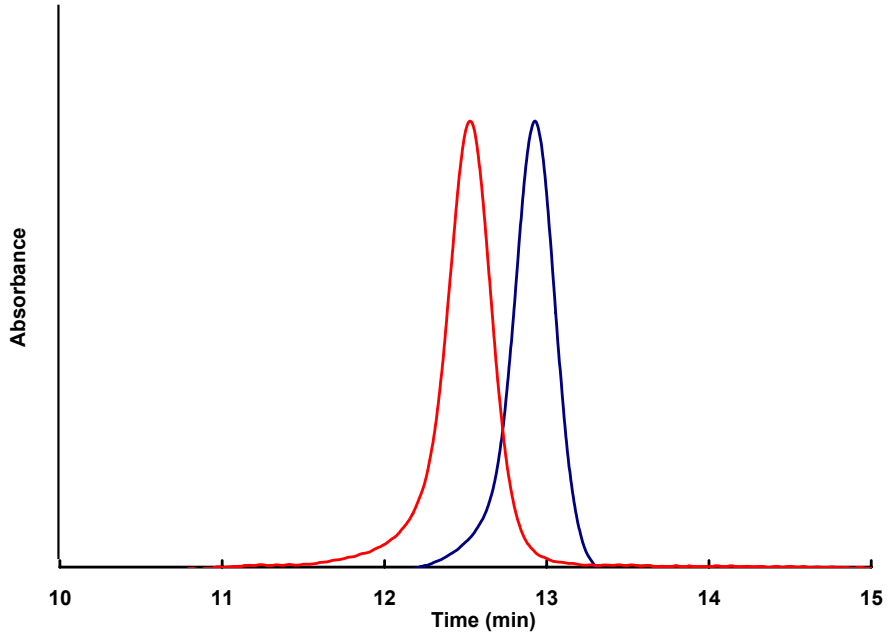

Figure 2.2. Normalized GPC traces for the isolated **N-EP5** (R.T. 12.93 min) and **N-EP6** (R.T. 12.53 min). Column: JAIGEL-3HA. Eluent: $CHCl_3$ with a flow rate = 1.2 ml/ min. Monitored at 420 nm.

These two peak components were easily separated by using preparative GPC, employing $CHCl_3$ as the eluent. Each fraction was concentrated and injected again into analytical GPC to confirm the clear separation and stability of the isolated macrocycles (Figure 2.2).

2.3- Covalent trapping of the macrorings. The complementary coordination of imidazolyl to zinc is strong enough (Ka~10^{11} M^{-1}) to maintain the structures of the isolated macrorings for several weeks in non-coordinating solvents (~10 μM) such as $CHCl_3$ (including 0.5% EtOH as a stabilizer) and toluene. However, in coordinating solvents (e.g. MeOH and pyridine) the self-assembled macrorings (**N-EP5** and **N-EP6**) can be dissociated into **Zn-EP-Zn** units by competitive coordination of the solvent. To obtain the permanent stability, the coordination pairs of these macrocycles were fixed by Grubbs' ring-closing metathesis reactions of *meso*-substituents (Scheme 4).[8e] Each covalently linked macroring was purified by preparative GPC with $CHCl_3$/MeOH (10/1) as an eluent, and its purity was checked by analytical GPC (Figure 2.3). Covalent linkage allows molecular weight determination by mass spectrometry (section 3.1), molecular visualization by STM (section 3.3) and photophysical measurements in coordinating solvents such as pyridine (Chapter 4).[15]

Scheme 4. Covalent linkage of the self-assembled rings **N-EP5** and **N-EP6**.

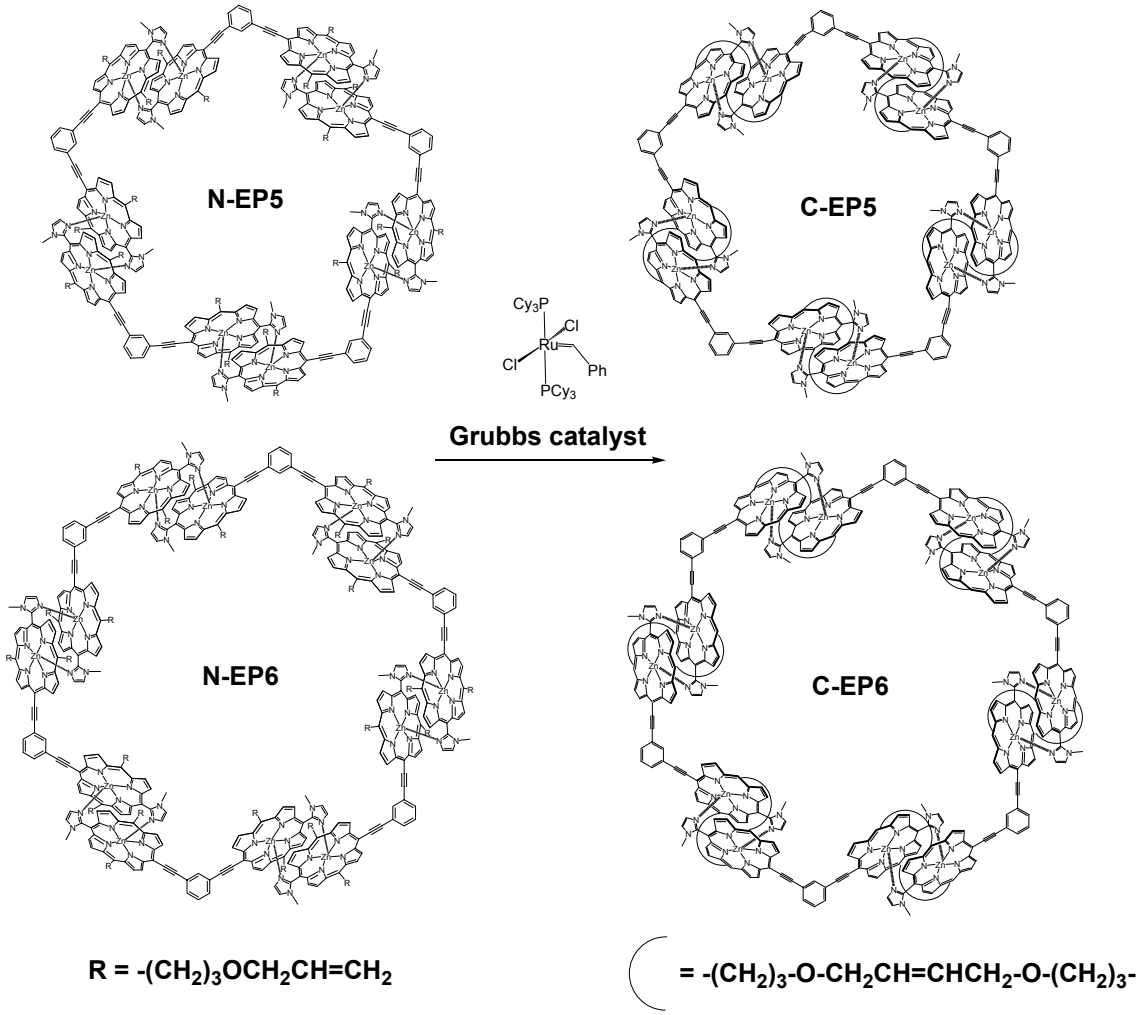

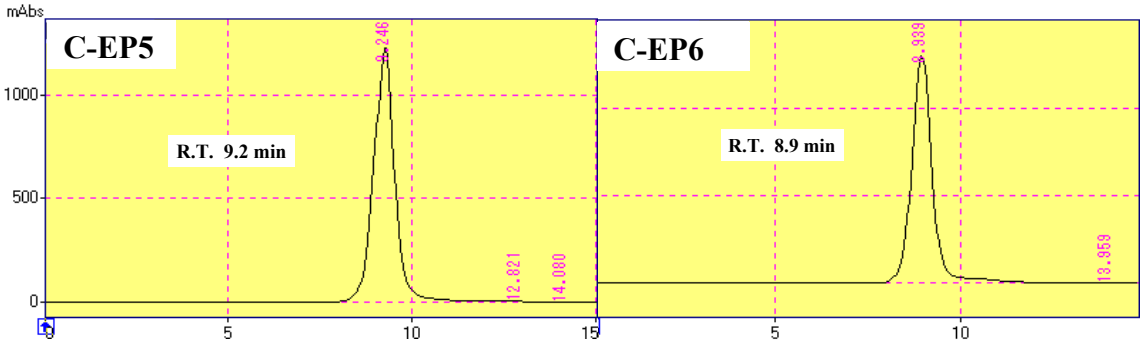

Figure 2.3. GPC traces for the covalently linked pentamer (**C-EP5**, R.T. 9.2 min) and hexamer (**C-EP6**, R.T. 8.9 min). Column: Tosoh GM2500H_{HR}. Eluent: pyridine with a flow rate = 0.8 ml/ min. Monitored at 420 nm.

2.4- Synthesis of benchmark porphyrins. To probe the electronic interactions in the macrorings (Chapter 4), two reference molecules, porphyrins **C-EP1** and **C-EP2** were prepared by mixing **Zn-EP** (3 equiv) and **Zn-EP-Zn** (1 equiv) in pyridine (Scheme 5). After pyridine removal, the GPC trace of the crude indicated the formation of mixed coordination oligomers of **Zn-EP**/(**Zn-EP-Zn**)n/**Zn-EP** (n = 0, 1, 2,..) (Figure 2.4 (a)). At this stage, the crude was dissolved in dichloromethane and subjected to the olefin metathesis reaction by the addition of Grubbs catalyst. Separation of these benchmarks was achieved on recycling GPC, employing pyridine as the eluent (Figure 2.4 (b)).

Scheme 5. Synthesis of porphyrin benchmarks.

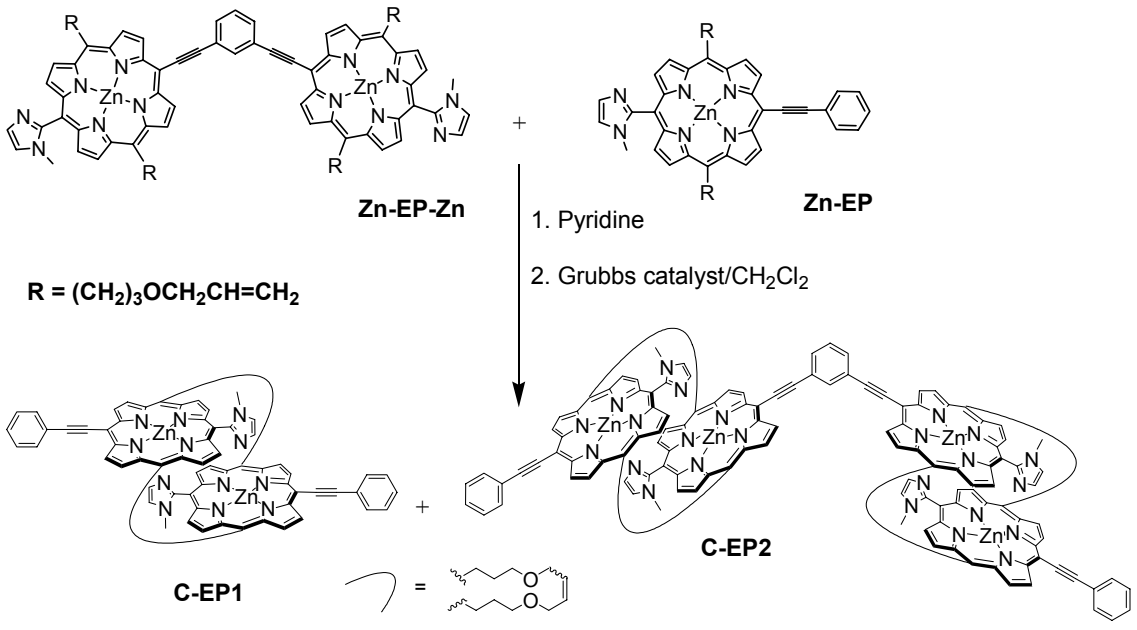

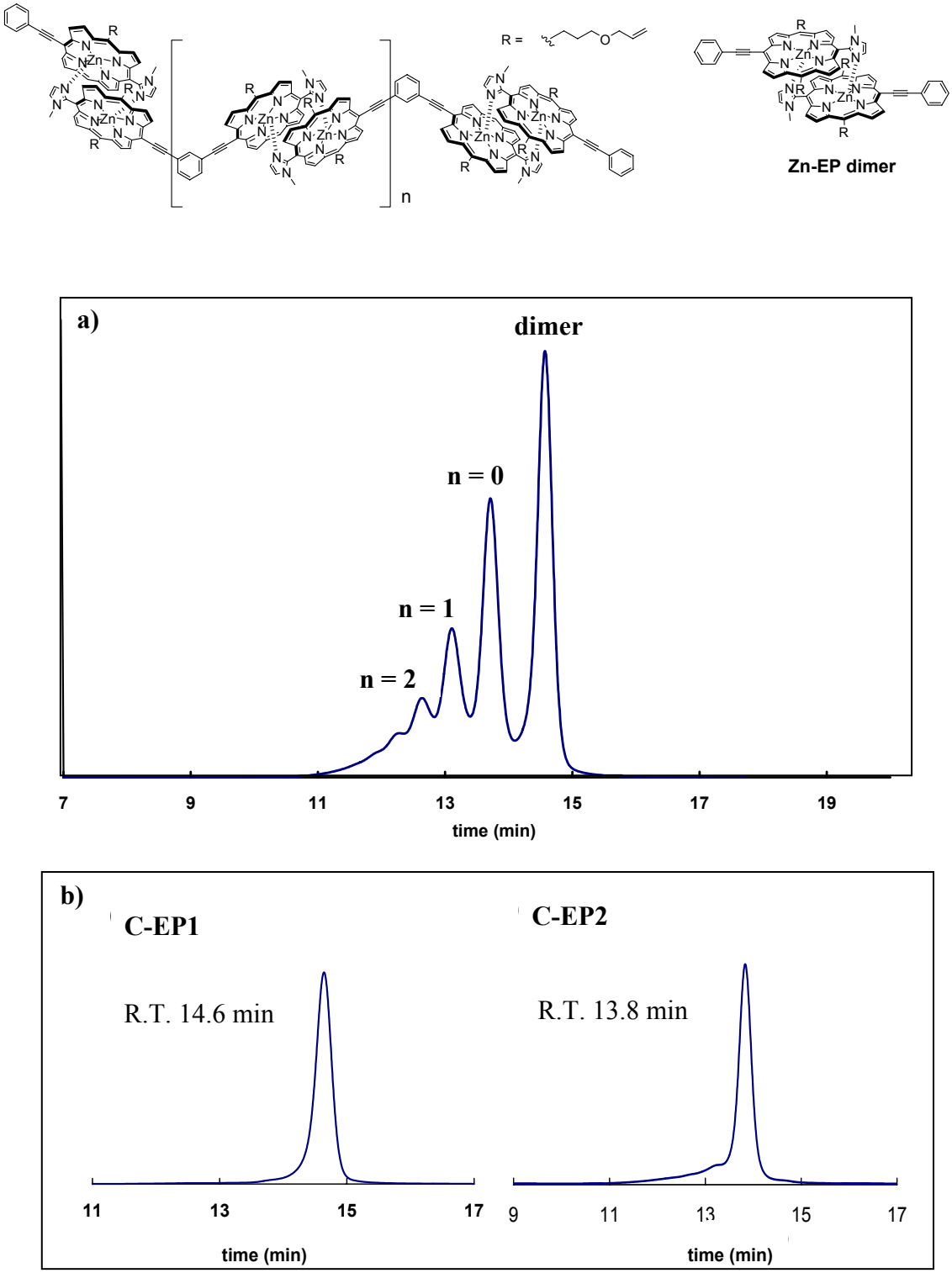

Figure 2.4. GPC traces. (a) Crude mixture of **Zn-EP** and **Zn-EP-Zn** after pyridine removal. (b) Purified **C-EP1** and **C-EP2**. Column: JAIGEL-3HA. Eluent: $CHCl_3$ with a flow rate = 1.2 ml/ min. Monitored at 420 nm.

2.5- Experimental section

Synthetic procedure of EP5, EP6 and reference porphyrins

General. All solvents and reagents were of reagent quality, purchased commercially, and used without further purification, except as noted below. Chloroform contained 0.5% ethanol as a stabilizer. Tetrahydrofuran (THF) was distilled from purple sodium benzophenone dianion solutions before use. Triethylamine (Et_3N) was distilled from calcium hydride before use. Tris(dibenzylideneacetone)dipalladium-chloroform complex (Pd_2dba_3), $AsPh_3$, tetrabutylammonium fluoride (*n*-Bu_4NF) and 1,3-diiodobenzene were obtained commercially from Aldrich. 1-methylimidazol-2-carboxaldehyde,[8e] 1-trimethylsilylethynylaldehyde,[13] and *meso*-(3-allyloxypropyl)dipyrromethane,[8e] were synthesized according to the published procedures. NMR spectra were recorded on a JEOL ECP-600 (600 MHz) spectrometer in $CDCl_3$ and with Me_4Si as an internal standard at 25°C unless otherwise noted. Chemical shift (δ) values are given in ppm. Mass spectra were measured by Perspective Biosystems Voyager DE-STR spectrometer with dithranol (Aldrich) as a matrix. Column chromatography was performed with silica gel (63-210 μm, KANTO chemical Co., Inc.). GPC-HPLC was performed on JAIGEL 3HA column (polystyrene gel, exclusion limit = 7×10^4 Dalton) with $CHCl_3$ as an eluent, and Tosoh TSK-GEL

G2500H_{HR} (polystyrene gel, exclusion limit = 2 × 10^4 Dalton) with pyridine as an eluent.

5,15-Bis(3-allyloxypropyl)-10-(trimethylsilylethynyl)-20-(1-methyl-2-imidazolyl) porphyrin (H_2-1). 1-Methylimidazol-2-carboxaldehyde (473.4 mg, 4.30 mmol), 1-trimethylsilylethynylaldehyde (271.35 mg, 2.15 mmol), and *meso*-(3-allyloxypropyl)dipyrromethane (1050.4 mg, 4.30 mmol) were dissolved in 1000 ml of $CHCl_3$ (N_2-purged). Trifluoroacetic acid (0.50 ml, 6.45 mmol) was added to the mixture, and the reaction mixture was stirred for 5 h at room temperature under N_2. 2,3-Dichloro-5,6-dicyano-1,4-benzoquinone (DDQ, 732.0 mg, 3.22 mmol) was added to the reaction mixture and stirred for 2 h. Triethylamine (0.8 ml, 5.74 mmol) was added to neutralize the reaction mixture, and all the solvents were removed under reduced pressure. The residue was purified by silica gel column chromatography (eluent: $CHCl_3$) to give **H_2-1** (110 mg, 7.5%).

^{1}H NMR (600 MHz, $CDCl_3$) δ 9.75, 9.53, 9.45, 8.73 (each d, 2H × 4, J = 4.8 Hz, pyrrole- H_β), 7.67 (s, 1H, imidazole-H_4), 7.45 (s, 1H, imidazole-H_5), 6.13-6.06 (m, 2H, CH_2=C<u>H</u>-), 5.43 (d, 2H, J = 17 Hz, C<u>H</u>$_2$=CH-), 5.28 (d, 2H, J = 10.2 Hz, C<u>H</u>$_2$=CH-), 5.05 (t, 4H, J = 7.5 Hz, CH_2), 4.09-4.06 (m, 4H, OCH_2), 3.65 (t, 4H, J = 5.7 Hz, CH_2),

3.38 (s, 3H, NCH_3), 2.79-2.74 (m, 4H, CH_2), 0.64 (s, 9H, $Si(CH_3)_3$), -2.49 (s, 2H, inner-NH). ^{13}C NMR (150 MHz, $CDCl_3$) δ 148.7 (C, imidazole-C_2), 147.5 (br, C, pyrrole-α), 135.0 (CH, allyl), 131.4, 130.8, 128.8, 128.6 (CH, pyrrole-β), 128.4 (CH, imidazole-C_4), 121.4 (CH, imidazole-C_5), 120.2 (C, *meso*), 116.9 (CH_2, allyl), 107.3 (C, *meso*), 106.2 (C, *meso*), 101.9 (C, ethyne), 99.5 (C, ethyne), 72.0 (CH_2, OCH_2), 69.1 (CH_2), 37.7 (CH_2), 34.5 (CH_3, NCH_3), 31.2 (CH_2), 0.54 (CH_3, $Si(CH_3)_3$). MS (MALDI-TOF, dithranol): Found *m/z* = 682.9 $[M+H]^+$, calcd for $C_{41}H_{46}N_6O_2Si$ 682.4. UV-vis (λ_{abs} (relative intensity), $CHCl_3$): 666 (0.03), 606.5 (0.01), 566.5 (0.06), 528 (0.04) and 427nm (1.00). Fluorescence, λ_{ex} = 427 nm, (λ_{max}, $CHCl_3$): 669.8, 739.0 nm.

5,15-Bis(3-allyloxypropyl)-10-ethynyl-20-(1-methyl-2-imidazolyl)porphyrin (H_2-2). To a solution of **H_2-1** (80.0 mg, 0.12 mmol) in 5.8 ml of $CHCl_3$ was added tetrabutylammonium fluoride (1 M in THF, 0.35 ml, 0.35 mmol), and the mixture was stirred for 30 min at room temperature. The reaction mixture was washed with water, dried over anhydrous $MgSO_4$ and concentrated. The crude product was purified by silica gel column chromatography ($CHCl_3$/ acetone 20:1) to yield 70.0 mg (98%) of **H_2-2** as a purple solid.

^{1}H NMR (600 MHz, $CDCl_3$) δ 9.68, 9.47, 9.44, 8.74 (each d, 2H × 4, *J* = 4.8 Hz, pyrrole- H_β), 7.67 (s, 1H, imidazole-H_4), 7.43 (s, 1H, imidazole-H_5), 6.11-6.05 (m, 2H, CH_2=C<u>H</u>-), 5.42 (d, 2H, *J* = 17.4 Hz, C<u>H</u>$_2$=CH-), 5.27 (d, 2H, *J* = 10.5 Hz, C<u>H</u>$_2$=CH-), 5.01-4.98 (m, 4H, CH_2), 4.17(s, 1H, C≡C<u>H</u>), 4.06-4.04 (m, 4H, OCH_2), 3.60 (t, 4H, *J* = 5.7 Hz, CH_2), 3.34 (s, 3H, NCH_3), 2.75-2.71 (m, 4H, CH_2), -2.59 (s, 2H, inner-NH). ^{13}C NMR (150 MHz, $CDCl_3$) δ 148.6 (C, imidazole-C_2), 147.5 (br, C, pyrrole-α), 135.0 (CH, allyl), 131.2, 130.9, 128.8, 128.6 (CH, pyrrole-β), 128.4 (CH, imidazole-C_4), 121.4 (CH, imidazole-C_5), 120.2 (C, *meso*), 116.9 (CH_2, allyl), 106.5 (C, *meso*), 97.9 (C, *meso*), 85.8 (C, ethyne), 84.0 (CH, ethyne), 72.0 (CH_2, OCH_2), 69.0 (CH_2), 37.7 (CH_2), 34.5 (CH_3, NCH_3), 31.1 (CH_2). MS (MALDI-TOF, dithranol): Found *m/z* = 611.0 $[M+H]^+$, calcd for $C_{38}H_{38}N_6O_2$ 610.3. UV-vis (λ_{abs} (relative intensity), $CHCl_3$): 661.5 (0.02), 603.5 (0.01), 561.5 (0.04), 524.5 (0.04), and 423.5 nm (1.00). Fluorescence, λ_{ex} = 423 nm, (λ_{max}, $CHCl_3$): 665.8, 735.6 nm.

5,15-Bis(3-allyloxypropyl)-10-(3-iodophenylethynyl)-20-(1-methyl-2-imidazolyl) porphyrin (H_2-3). Air was removed from a solution of **H_2-2** (58.0 mg, 95.0 μmol) and 1,3-diiodobenzene (125.0 mg, 0.38 mmol) in 46 ml of THF/Et_3N (5:1) by blowing argon for 30 min. Then, Pd_2dba_3 (29.5 mg, 28.5 μmol) and $AsPh_3$ (58.2 mg, 0.19 mmol)

were added, and the reaction mixture was stirred at room temperature under argon. After 24 h, water was added to quench the reaction. The organic layer was separated, washed with saturated $NaHCO_3$ aqueous solution, and dried over anhydrous $MgSO_4$. The solvent was removed in vacuo, and the residue was purified by silica gel column chromatography ($CHCl_3$/ acetone 50:1) to yield 60 mg (78 %) of **H_2-3**.

^{1}H NMR (600 MHz, $CDCl_3$) δ 9.61, 9.42, 9.40, 8.72 (each d, 2H × 4, J = 4.8 Hz, pyrrole- H_β), 8.38 (s, 1H, Ph-H), 7.95 (d, 1H, J = 7.8 Hz, Ph-H), 7.82 (d, 1H, J = 7.8 Hz, Ph-H), 7.69 (s, 1H, imidazole-H_4), 7.44 (s, 1H, imidazole-H_5), 7.28 (t, 1H, J = 7.8 Hz, Ph-H), 6.12-6.05 (m, 2H, CH_2=C<u>H</u>-), 5.42 (d, 2H, J = 13.8 Hz, C<u>H_2</u>=CH-), 5.27 (d, 2H, J = 10.8 Hz, C<u>H_2</u>=CH-), 4.97-4.91 (m, 4H, CH_2), 4.09-4.04 (m, 4H, OCH_2), 3.60 (t, 4H, J = 5.7 Hz, CH_2), 3.36 (s, 3H, NCH_3), 2.73-2.69 (m, 4H, CH_2), -2.56 (s, 2H, inner-NH). ^{13}C NMR (150 MHz, $CDCl_3$) δ 148.6 (C, imidazole-C_2), 148.2-145.6 (br, C, pyrrole-α), 140.0 (C, Ph), 137.5 (CH, Ph), 135.0 (CH, allyl), 131.0, 130.6 (each br, CH, pyrrole-β), 130.2 (CH, Ph), 129.0, 128.6 (each br, CH, pyrrole-β), 128.5 (CH, Ph), 126.1 (CH, imidazole-C_4), 121.4 (CH, imidazole-C_5), 120.3, 120.0 (C, *meso*), 116.8 (CH_2, allyl), 106.4 (C, *meso*), 101.5 (CH, Ph), 98.9 (C, *meso*), 94.7 (C, Ph), 94.0, 93.6 (C, ethyne), 72.1 (CH_2, OCH_2), 69.2 (CH_2), 37.7 (CH_2), 34.5 (CH_3, NCH_3), 31.2 (CH_2). MS (MALDI-TOF, dithranol): Found m/z = 812.6 $[M+H]^+$, calcd for $C_{44}H_{41}IN_6O_2$ 812.2.

UV-vis (λ_{abs} (relative intensity), $CHCl_3$): 672 (0.05), 610 (0.02), 575 (0.09), 532.5 (0.03) and 433 nm (1.00). Fluorescence, λ_{ex} = 433 nm, (λ_{max}, $CHCl_3$): 676.2, 744.4 nm.

5,15-Bis(3-allyloxypropyl)-10-(3-iodophenylethynyl)-20-(1-methyl-2-imidazolyl) porphyrinatozinc(II) (Zn-3). A solution of zinc acetate dihydrate (716.0 mg, 3.26 mmol) in 6 ml of methanol was added to a solution of **H_2-3** (53.0 mg, 62.2 μmol) in 25 ml of chloroform. The mixture was stirred at room temperature for 2 h. The mixture was then washed with saturated $NaHCO_3$ aqueous solution followed by drying over anhydrous $MgSO_4$ and concentration under reduced pressure. The crude product was purified by silica gel column chromatography ($CHCl_3$/ acetone 40:1) to yield **Zn-3** (50 mg, 92%).

^{1}H NMR (600 MHz, $CDCl_3$) of **Zn-3** dimer: δ 9.95 (d, 2H, *J* = 4.2 Hz, pyrrole- H_β), 9.73 (d, 2H, *J* = 4.2 Hz, pyrrole- H_β), 8.90 (d, 2H, *J* = 4.2 Hz, pyrrole- H_β), 8.55 (s, 1H, Ph-H), 8.15 (d, 1H, *J* = 7.8 Hz, Ph-H), 7.88 (d, 1H, *J* = 7.8 Hz, Ph-H), 7.40 (t, 1H, *J* = 7.8 Hz, Ph-H), 6.24-6.17 (m, 2H, CH_2=C<u>H</u>-), 5.55 (d, 2H, *J* = 17.4 Hz, C<u>H_2</u>=CH-), 5.51 (s, 1H, imidazole-H_5), 5.42 (d, 2H, *J* = 4.2 Hz, pyrrole- H_β), 5.37 (d, 2H, *J* = 10.2 Hz, C<u>H_2</u>=CH-), 5.22-5.17 (m, 4H, CH_2), 4.29-4.20 (m, 4H, CH_2), 3.94-3.89 (m, 4H, OCH_2), 3.08-2.99 (m, 4H, CH_2), 2.09 (s, 1H, imidazole-H_4), 1.69 (s, 3H, NCH_3).

^{13}C NMR (150 MHz, $CDCl_3$) δ 151.4, 150.8, 150.4, 147.5 (C, pyrrole-α), 145.6 (C, imidazole-C_2), 140.0 (C, Ph), 137.0 (CH, Ph), 135.3 (CH, allyl), 131.0, 130.6 (CH, pyrrole-β), 130.2 (CH, Ph), 129.6, 129.2 (CH, pyrrole-β), 127.4 (CH, Ph), 127.0 (C, *meso*), 121.8 (CH, imidazole-C_4), 120.4 (C, *meso*), 118.0 (CH, imidazole-C_5), 116.8 (CH_2, allyl), 101.4 (CH, Ph), 98.6 (C, *meso*), 96.0 (C, Ph), 94.2, 93.6 (C, ethyne), 72.1 (CH_2, OCH_2), 68.8 (CH_2), 38.5 (CH_2), 32.6 (CH_3, NCH_3), 32.0 (CH_2). MS (MALDI-TOF, dithranol): Found *m/z* 874.8 $[M+H]^+$, calcd for $C_{44}H_{39}IN_6O_2Zn$ 874.2. UV-vis (λ_{abs} (relative intensity), $CHCl_3$): 651 (0.21), 582 (0.04), 453 (1.00) and 430.5 nm (0.49). Fluorescence, λ_{ex} = 453 nm, (λ_{max}, $CHCl_3$): 656.4, 716.4 nm.

1-[5',15'-Bis(3-allyloxypropyl)-10'-(1-methyl-2-imidazolyl)-20'-ethynylporphinyl]-3-[zinc(II)-5,15-bis(3-allyloxypropyl)-10-(1-methyl-2-imidazolyl)-20-ethynylporphinyl]-benzene (H_2-EP-Zn). Zn-3 (100.0 mg, 0.11 mmol) and **H_2-2** (70.0 mg, 0.11 mmol) were dissolved in 120 ml of THF/Et_3N (5:1) under argon. Pd_2dba_3 (18.9 mg, 18.3 μmol) and $AsPh_3$ (44.7 mg, 0.12 mmol) were added to the mixture, and the mixture was stirred at room temperature under argon. After 24 h, the crude mixture was diluted with $CHCl_3$ (50 ml), washed with water, dried over anhydrous $MgSO_4$, filtered and concentrated. The residue was loaded on a silica column and eluted with $CHCl_3$/MeOH

(10:1). Further purification using preparative GPC column (Tosoh GM2500H_{HR}, pyridine) afforded **H_2-EP-Zn** (75 mg, 50%), **H_2-EP** (10%) and a negligible amount of **4**. ^{1}H NMR (600 MHz, $CDCl_3$) of **H_2-EP-Zn** dimer: δ 10.15 (d, 4H, *J* = 4.2 Hz, pyrrole-H_β), 10.04 (d, 4H, *J* = 4.2 Hz, pyrrole-H_β), 9.82-9.78 (m, 4H, pyrrole-H_β), 9.68 (d, 4H, *J* = 4.2 Hz, pyrrole-H_β), 9.50 (d, 4H, *J* = 4.2 Hz, pyrrole-H_β), 8.95 (d, 4H, *J* = 4.2 Hz, pyrrole-H_β), 8.91 (s, 2H, Ph-H), 8.77 (br, 4H, pyrrole-H_β), 8.37 (d, 2H, *J* = 7.2 Hz, Ph-H), 8.27 (d, 2H, *J* = 7.2 Hz, Ph-H), 7.92 (t, 2H, *J* = 7.2 Hz, Ph-H), 7.70 (s, 2H, imidazole-H_4), 7.49 (s, 2H, imidazole-H_5), 6.26-6.19 (m, 4H, CH_2=C<u>H</u>-), 6.17-6.10 (m, 4H, CH_2=C<u>H</u>-), 5.56 (d, 4H, *J* = 15 Hz, C<u>H</u>$_2$=CH-), 5.49 (s, 2H, imidazole-H_5), 5.47 (d, 8H, *J* = 13.8 Hz, C<u>H</u>$_2$=CH-), 5.37 (d, 4H, *J* = 4.2 Hz, pyrrole-H_β), 5.32 (d, 4H, *J* = 10.2 Hz, C<u>H</u>$_2$=CH-), 5.29-5.19 (m, 8H, CH_2), 5.12 (t, 8H, *J* = 7.2 Hz, CH_2), 4.35-4.26 (m, 8H, OCH_2), 4.16-4.11 (m, 8H, OCH_2), 3.99-3.92 (m, 8H, CH_2), 3.71 (t, 8H, *J* = 5.4 Hz, CH_2), 3.43 (s, 6H, NCH_3), 3.16-3.02 (m, 8H, CH_2), 2.85-2.83 (m, 8H, CH_2), 2.21 (s, 2H, imidazole-H_4), 1.73 (s, 6H, NCH_3), -2.25 (s, 4H, inner-NH). ^{13}C NMR (150 MHz, $CDCl_3$) δ 151.5, 150.9, 150.5, 147.6 (C, pyrrole-α), 148.6, 145.8 (C, imidazole-C_2), 135.4, 135.1 (CH, allyl), 134.4 (CH, Ph), 131.8, 131.3, 131.1 (CH, pyrrole-β), 131.0 (CH, Ph), 129.7, 129.3, 128.9 (CH, pyrrole-β), 127.5 (CH, imidazole-C_4), 125.7 (C, *meso*), 124.7 (CH, Ph), 121.9 (CH, imidazole-C_4), 121.5 (CH, imidazole-C_5), 120.5,

120.4, 120.1 (C, *meso*), 118.0 (CH, imidazole-C_5), 116.9 (CH_2, allyl), 105.9 (C, *meso*), 101.4 (CH, Ph), 99.8, 99.0 (C, Ph), 98.9, 98.6 (C, *meso*), 96.3, 95.5, 94.7, 93.2 (C, ethyne), 72.1, 72.0 (CH_2, OCH_2), 70.0, 69.1 (CH_2), 38.5, 37.8 (CH_2), 34.4, 32.7 (CH_3, NCH_3), 31.2, 30.1 (CH_2). MS (MALDI-TOF, dithranol): Found *m/z* 1357.2 $[M+H]^+$, calcd for $C_{82}H_{76}N_{12}O_4Zn$ 1356.5. UV-vis (λ_{abs} (relative intensity), $CHCl_3$): 677 (0.07), 653 (0.15), 582 (0.10), 534.5 (0.04), 456 (1.00), and 430.5 (0.81) nm. Fluorescence, λ_{ex} = 456 nm, (λ_{max}, $CHCl_3$): 676.6, 743.6 nm.

5,15-Bis(3-allyloxypropyl)-10-(phenylethynyl)-20-(1-methyl-2-imidazolyl)porphyrinatozinc(II) (Zn-EP). H_2-EP was metalated with zinc acetate dihydrate under similar condition applied for **Zn-3**.

^{1}H NMR (600 MHz, $CDCl_3$) of **Zn-EP** dimer: δ 10.0 (d, 2H, *J* = 4.2 Hz, pyrrole- H_β), 9.72 (d, 2H, *J* = 4.8 Hz, pyrrole- H_β), 8.89 (d, 2H, *J* = 4.2 Hz, pyrrole- H_β), 8.21 (d, 2H, *J* = 7.2 Hz, Ph-H), 7.66 (m, 2H, Ph-H), 7.55 (m, 1H, Ph-H), 6.24-6.18 (m, 2H, CH_2=C<u>H</u>-), 5.54 (d, 2H, *J* = 17.1 Hz, C<u>H$_2$</u>=CH-), 5.48 (s, 1H, imidazole-H_5), 5.41 (d, 2H, *J* = 4.2 Hz, pyrrole- H_β), 5.36 (d, 2H, *J* = 10.2 Hz, C<u>H$_2$</u>=CH-), 5.24-5.16 (m, 4H, CH_2), 4.24-4.23 (m, 4H, CH_2), 3.94-3.87 (m, 4H, OCH_2), 3.09-2.97 (m, 4H, CH_2), 2.11 (s, 1H, imidazole-H_4), 1.67 (s, 3H, NCH_3). ^{13}C NMR (150 MHz, $CDCl_3$) δ 151.4, 150.8,

150.3, 147.6 (C, pyrrole-α), 145.7 (C, imidazole-C_2), 135.3 (CH, allyl), 131.6 (C, Ph), 131.0, 129.4, 129.1, 128.8 (CH, pyrrole-β), 128.1 (CH, Ph), 127.3 (C, *meso*), 124.9 (CH, Ph), 121.8 (CH, imidazole-C_4), 120.2 (C, *meso*), 117.9 (CH, imidazole-C_5), 116.8 (CH_2, allyl), 99.4 (CH, Ph), 98.3 (C, *meso*), 95.3, 94.4 (C, ethyne), 72.1 (CH_2, OCH_2), 69.9 (CH_2), 38.5 (CH_2), 32.6 (CH_3, NCH_3), 32.1 (CH_2). MS (MALDI-TOF, dithranol): Found *m/z* 748.6 $[M+H]^+$, calcd for $C_{44}H_{40}N_6O_2Zn$ 748.2.UV-vis (λ_{abs} (relative intensity), $CHCl_3$): 649 (0.18), 581.5 (0.05), 451(1.00), and 431 (0.57) nm. Fluorescence, λ_{ex} = 451 nm, (λ_{max}, $CHCl_3$): 654, 713 nm.

1,3-Bis[zinc(II)-5,15-Bis(3-allyloxypropyl)-10-(1-methyl-2-imidazolyl)-20-ethynyl-porphinyl]benzene (Zn-EP-Zn). Zinc acetate dihydrate (72.7 mg, 0.33 mmol) dissolved in methanol (1.7 ml) was added to a chloroform solution (35 ml) of **H_2-EP-Zn** (15.0 mg, 11.0 μmol) and stirred for 2 h. The reaction mixture was diluted with chloroform (10 ml) and washed with saturated $NaHCO_3$ aqueous solution and water. The organic layer was dried over anhydrous $MgSO_4$ and evaporated to dryness. The residue was purified by reprecipitation (chloroform/*n*-hexane) to give 15 mg (96%) of **Zn-EP-Zn.** Analytical GPC analysis is shown in Figure 2.1 (red curve). MS (MALDI-TOF, dithranol): Found *m/z* 1419.3 $[M+H]^+$, calcd for $C_{82}H_{74}N_{12}O_4Zn_2$ 1418.4

Reorganization procedure. The above **Zn-EP-Zn** (15.0 mg, 10.5 μmol) was dissolved in 525 ml of $CHCl_3$/MeOH (10:1). The solution was kept in the dark at room temperature for 24 h, and then evaporated at 26°C under reduced pressure. The reorganized **Zn-EP-Zn** was used for later ring closing metathesis reaction. The obtained residue showed convergent GPC chromatogram (Figure 2.1, blue curve) with two peaks. The two components were separated by preparative GPC (JAIGEL 3HA, eluent: $CHCl_3$) to give **N-EP6** (6.0 mg, 40%) as the first fraction and **N-EP5** (5.2 mg, 35%) as the second fraction.

Pentameric ring (N-EP5). ^{1}H NMR (600 MHz, $CDCl_3$) δ 10.24 (d, 4H, *J* = 3.6 Hz, pyrrole-H_β), 9.88 (d, 4H, *J* = 3.6 Hz, pyrrole- H_β), 9.12 (s, 1H, Ph-H), 8.98 (d, 4H, *J* = 3.6 Hz, pyrrole-H_β), 8.35 (d, 2H, *J* = 6.6 Hz, Ph-H), 7.97 (t, 1H, *J* = 6.6 Hz, Ph-H), 6.29-6.22 (m, 4H, CH_2=C<u>H</u>-), 5.61 (d, 4H, *J* = 9.6 Hz, C<u>H</u>$_2$=CH-), 5.58 (s, 2H, imidazole-H_5), 5.52 (d, 4H, *J* = 3.6 Hz, pyrrole-H_β), 5.40 (d, 4H, *J* = 10.2 Hz, C<u>H</u>$_2$=CH-), 5.29 (br, 8H, CH_2), 4.30 (d, 8H, *J* = 5.4 Hz, CH_2), 4.02-3.95 (m, 8H, OCH_2), 3.17-3.08 (m, 8H, CH_2), 2.26 (s, 2H, imidazole-H_4), 1.77 (s, 6H, NCH_3). UV-vis (λ_{abs} (relative intensity), toluene): 656.5 (0.24), 582 (0.05), 459.0 (1.00), 442.5 (0.50) and 431.5 (0.48) nm. Fluorescence, λ_{ex} = 459 nm, (λ_{max}, toluene): 659.2, 720.2 nm.

GPC analysis (JAIGEL 3HA, eluent: $CHCl_3$ with flow rate = 1.2 ml/min at 25°C), retention time 12.93 min.

Hexameric ring (N-EP6). ^{1}H NMR (600 MHz, $CDCl_3$) δ 10.24 (d, 4H, *J* = 3.6 Hz, pyrrole-H_β), 9.88 (d, 4H, *J* = 3.6 Hz, pyrrole- H_β), 9.07 (s, 1H, Ph-H), 8.98 (d, 4H, *J* = 3.6 Hz, pyrrole-H_β), 8.38 (d, 2H, *J* = 6.6 Hz, Ph-H), 7.98 (t, 1H, *J* = 6.6 Hz, Ph-H), 6.30-6.23 (m, 4H, CH_2=C<u>H</u>-), 5.62 (s, 4H, C<u>H</u>$_2$=CH-), 5.59 (s, 2H, imidazole-H_5), 5.52 (d, 4H, *J* = 3.6 Hz, pyrrole-H_β), 5.41 (d, 4H, *J* = 10.2 Hz, C<u>H</u>$_2$=CH-), 5.29 (br, 8H, CH_2), 4.31 (d, 8H, *J* = 5.4 Hz, CH_2), 4.03-3.96 (m, 8H, OCH_2), 3.17-3.08 (m, 8H, CH_2), 2.26 (s, 2H, imidazole-H_4), 1.77 (s, 6H, NCH_3). UV-vis (λ_{abs} (relative intensity), toluene): 657 (0.25), 583.5 (0.05), 460.5 (1.00), 442 (0.49) and 431 (0.47) nm. Fluorescence, λ_{ex} = 459 nm, (λ_{max}, toluene): 659.4, 722.4 nm.

GPC analysis (JAIGEL 3HA, eluent: $CHCl_3$ with flow rate = 1.2 ml/min at 25°C), retention time 12.53 min.

Ring closing metathesis reaction. Reorganized **Zn-EP-Zn** (mixture of **N-EP5** and **N-EP6**, 7.0 mg, 4.92 μmol) was dissolved in CH_2Cl_2 (25 ml) and Grubbs catalyst (Fluka) (4.0 mg, 4.86 μmol) was added. The reaction mixture was stirred at room temperature under nitrogen atmosphere for 6 h. After quenching with water, the mixture was extracted with $CHCl_3$, dried over anhydrous $MgSO_4$ and evaporated to dryness.

Residue was passed through a short silica column and eluted with $CHCl_3$/MeOH (5:1). Finally, the mixture was purified by recycling GPC (Tosoh GM2500H_{HR} with $CHCl_3$/MeOH (10:1) as an eluent) to give the covalently linked macrorings, **C-EP6** (1.0 mg, 15%) as the first fraction and **C-EP5** (1.5 mg, 22%) as the second fraction.

C-EP5: MS (MALDI-TOF, dithranol): Found *m/z* 6832.7 $[M+H]^+$, calcd for $C_{390}H_{330}N_{60}O_{20}Zn_{10}$ 6831.1. GPC-HPLC analysis (Tosoh GM2500H_{HR} column, eluent: pyridine with flow rate = 0.8 ml/min at 25°C) retention time 9.2 min.

C-EP6: MS (MALDI-TOF, dithranol): Found *m/z* 8198.6 $[M+H]^+$, calcd for $C_{468}H_{396}N_{72}O_{24}Zn_{12}$ 8197.3. GPC-HPLC analysis (Tosoh GM2500H_{HR} column, eluent: pyridine with flow rate = 0.8 ml/min at 25°C) retention time 8.9 min.

Preparation of the benchmarks (C-EP1) and (C-EP2). Zn-EP-Zn (5 mg, 3.52 μmol) and **Zn-EP** (7.5 mg, 10 μmol) were dissolved in pyridine and concentrated at 40°C. At this stage, formation of mixed coordination oligomers of **Zn-EP/ (Zn-EP-Zn)n /Zn-EP** (n = 0, 1, 2,..) was confirmed by analytical GPC (Figure 2.4 (a)). The mixture was dissolved in CH_2Cl_2 (27 ml), and Grubbs catalyst (Fluka) (8.2 mg, 10 μmol) was added. The mixture was stirred at room temperature under nitrogen atmosphere for 4 h. After quenching with water, the reaction mixture was extracted with $CHCl_3$, dried over

anhydrous $MgSO_4$ and evaporated to dryness. Residue was loaded onto a short silica column and eluted with $CHCl_3$/MeOH (5:1) to remove non-porphyrin species as well as some high-molecular weight materials. Finally, the mixture of covalently linked oligomers was separated by using recycling GPC (Tosoh GM2500H_{HR} with pyridine as an eluent) to give **C-EP1** (8 mg, 79 %) and **C-EP2** (7.2 mg, 73 %). **C-EP1** and **C-EP2** include geometrical isomers concerning with the olefin parts.

C-EP1: ^{1}H NMR (600 MHz, $CDCl_3$) δ 10.0-9.98 (2H, pyrrole-H_β), 9.65-9.62 (2H, pyrrole-H_β), 9.03-8.93 (2H, pyrrole-H_β), 8.20 (2H, Ph-H), 7.66 (2H, Ph-H), 7.56 (1H, Ph-H), 6.45 (1.5H, CH=CH-), 6.11 (0.5H, CH=CH-), 5.50-5.47 (1H, imidazole-H_5), 5.44-5.35 (2H, pyrrole-H_β), 5.19-5.05 (3H, CH_2), 4.68 (1H, CH_2), 4.46-4.41 (4H, CH_2), 4.29-4.20 (4H, OCH_2), 3.14-2.97 (4H, CH_2), 2.09-2.07 (1H, imidazole-H_4), 1.71 (2H, NCH_3), 1.69 (1H, NCH_3).

GPC-HPLC analysis (JAIGEL 3HA, eluent: $CHCl_3$ with flow rate = 1.2 ml/min at 25°C), retention time 14.6 min. MS (MALDI-TOF, dithranol): Found *m/z* 1440.9 $[M+H]^+$, calcd for $C_{84}H_{72}N_{12}O_4Zn_2$ 1440.44.

C-EP2: ^{1}H NMR (600 MHz, $CDCl_3$) δ 10.22-10.19 (4H, pyrrole-H_β), 10.03-10.00 (4H, pyrrole-H_β), 9.78-9.76 (4H, pyrrole-H_β), 9.67-9.64 (4H, pyrrole-H_β), 9.08-8.98 (8H, pyrrole-H_β), 9.02 (1H, Ph-H), 8.38-8.37 (2H, Ph-H), 8.22-8.20 (4H, Ph-H), 7.97-7.95

(1H, Ph-H), 7.68-7.66 (4H, Ph-H), 7.57-7.55 (2H, Ph-H), 6.48 (7H, CH=CH-), 6.14 (1H, CH=CH-), 5.60-5.51 (4H, imidazole-H_5), 5.50-5.37 (8H, pyrrole-H_β), 5.26-5.08 (14H, CH_2), 4.72 (2H, CH_2), 4.49-4.41 (16H, CH_2), 4.29-4.22 (16H, OCH_2), 3.20-3.01 (16H, CH_2), 2.22-2.19 (2H, imidazole-H_4), 2.12-2.09 (2H, imidazole-H_4), 1.76-1.73 (12H, NCH_3).

GPC-HPLC analysis (JAIGEL 3HA, eluent: $CHCl_3$ with flow rate = 1.2 ml/min at 25°C), retention time 13.8 min. MS (MALDI-TOF, dithranol): Found *m/z* 2802.7 $[M+H]^+$, calcd for $C_{162}H_{138}N_{24}O_8Zn_4$ 2802.83.

Chapter 3- Structural Characterization of the Macrorings in Solution and Solid-State

3.1- Mass spectrometry. MALDI-TOF mass spectrometry is a powerful method to obtain direct evidence of the exact molecular weight. Even though the complementary coordination is strong enough to retain the cyclic structures of **N-EP5** and **N-EP6** in solution, the ionization conditions in mass spectrometry are too harsh and afforded predominantly dissociated monomeric peaks. As discussed in section 2.3, covalent linkage of the macrocycles was attempted by means of Grubbs' ring-closing metathesis reaction. It enabled the detection of molecular-ion peaks corresponding to the covalently linked **C-EP5** (Found *m/z* 6832, calcd. 6831) and **C-EP6** (Found *m/z* 8198, calcd. 8197) in mass spectrometry, thus, proving the formation of the target macrocycles (Figure 3.1).

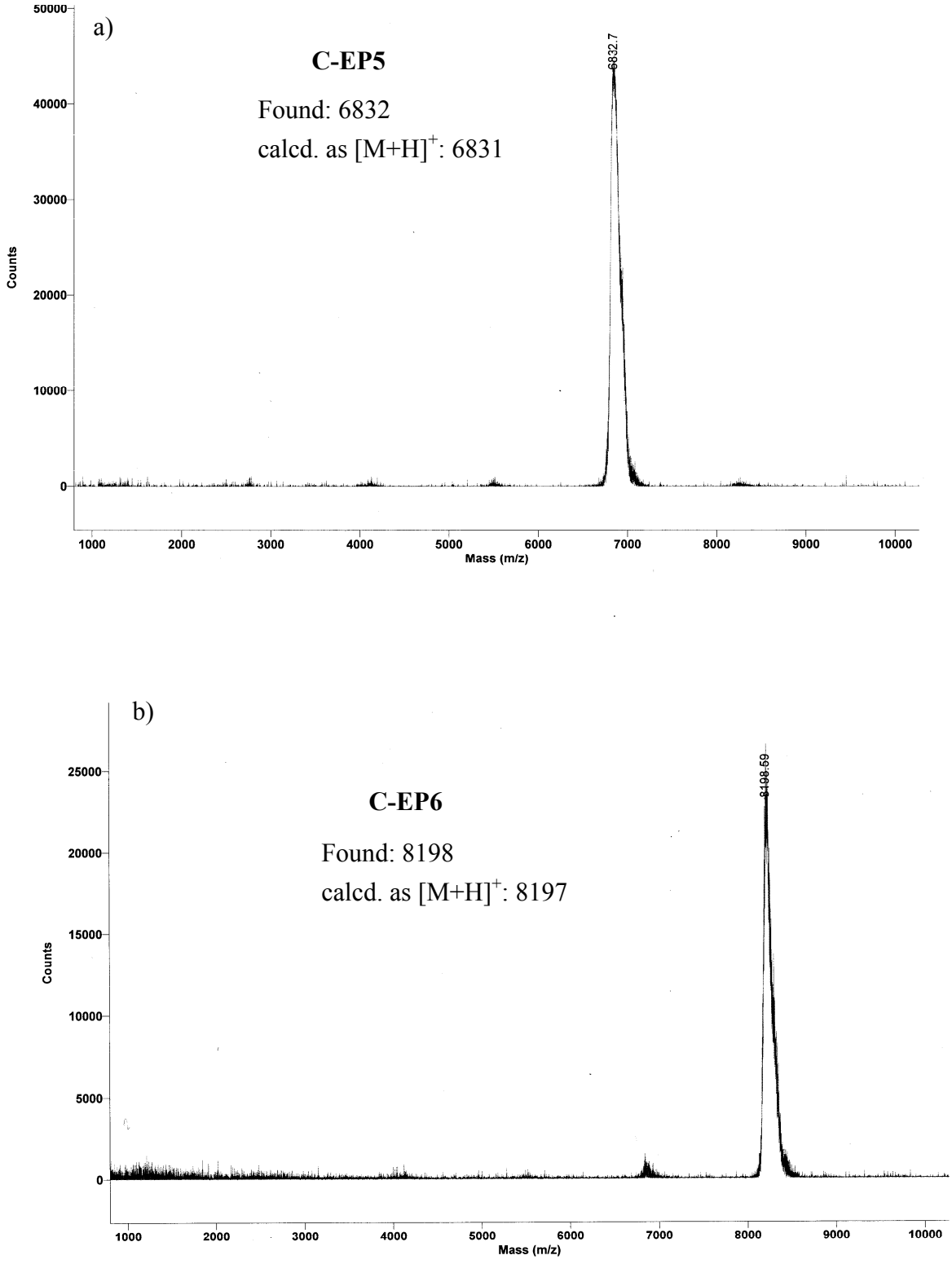

Figure 3. 1. MALDI-TOF mass spectra of (a) **C-EP5** and (b) **C-EP6**.

3.2- ^{1}H NMR spectroscopy. The cyclic structure of the macrorings, **N-EP5** and **N-EP6**, can be easily confirmed by ^{1}H NMR. Figure 3.2 shows ^{1}H NMR spectra of **H_2-3**, **Zn-3**, **N-EP5** and **N-EP6** in $CDCl_3$ at room temperature. Due to dimer formation, protons Im_5, Im_4, *N*-Me, β_1 and β_2 of **Zn-3** are considerably upfield shifted to 5.51, 2.09, 1.69, 5.42, and 8.90 ppm, respectively, compared to the corresponding peaks of **H_2-3**. By contrast, β_3 and β_4 protons of **Zn-3** are downfield shifted as a result of the deshielding effect of the counterpart porphyrin. This shift behavior is consistent with the previous observations of zinc imidazolylporphyrin dimer.[16]

As can be seen in Figure 3.2 (spectra C and D), the ^{1}H NMR spectra of the macrorings are clearly-resolved and exhibited only a single set of porphyrin protons, which resembles that of the dimeric precursor **Zn-3**. However, due to the influence of the ring current effect, all the proton resonances in **N-EP5** and **N-EP6** were shifted downfield relative to **Zn-3** and only the phenyl protons show remarkable difference associated with phenylethynyl substitution framework. Importantly, the imidazolyl protons Im_5, Im_4 and *N*-Me of the macrorings appeared at 5.58, 2.26 and 1.77 ppm, respectively, are diagnostic feature of complementary dimer formation.[8b, c]

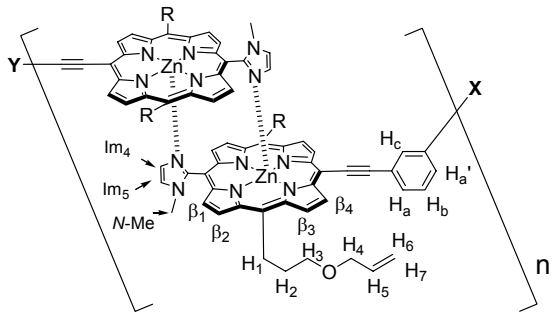

Zn-3 dimer: X = I, Y = 3-I-C_6H_4-, n=1
N-EP5: X - Y, n= 5
N-EP6: X - Y, n= 6

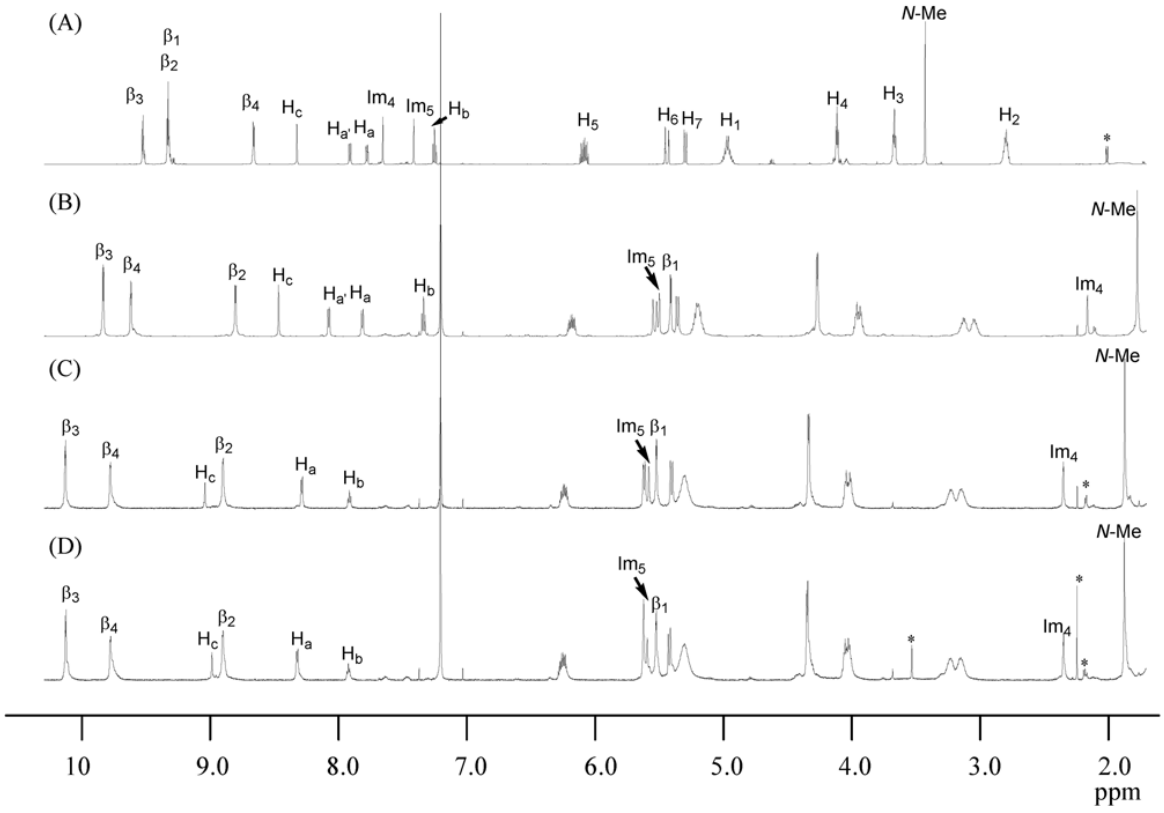

Figure 3.2. ^{1}H NMR spectra of (A) **H_2-3**, (B) **Zn-3**, (C) **N-EP5**, and (D) **N-EP6** in $CDCl_3$ at ambient temperature. (*) denotes impurity peaks. The assignments in spectra C and D are based on ^{1}H-^{1}H COSY and HMQC experiments (Figures 3.3 and 3.4).

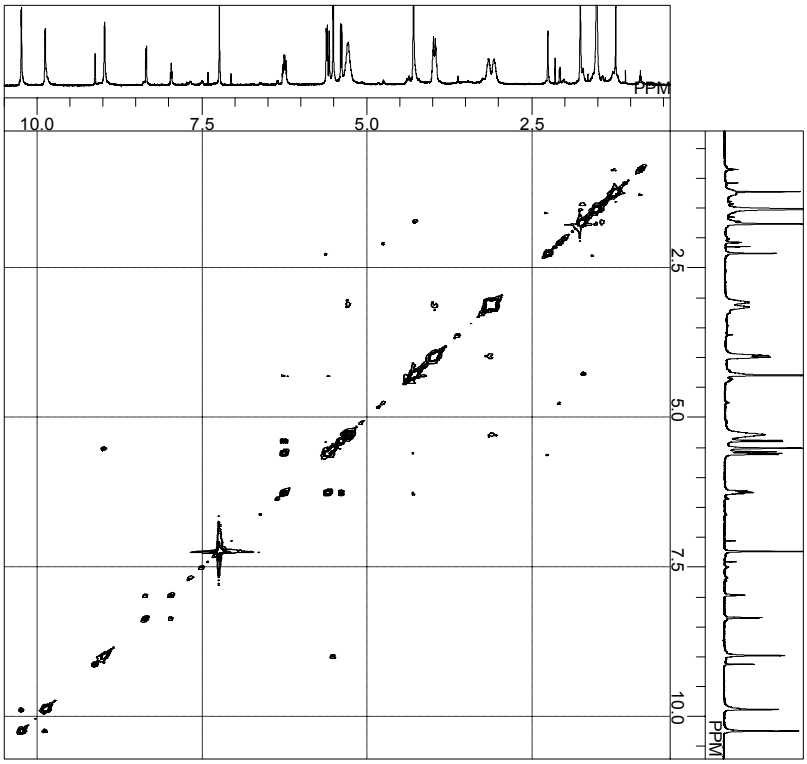

Figure 3.3. ^{1}H-^{1}H COSY spectrum of **N-EP5** in $CDCl_3$ at room temperature.

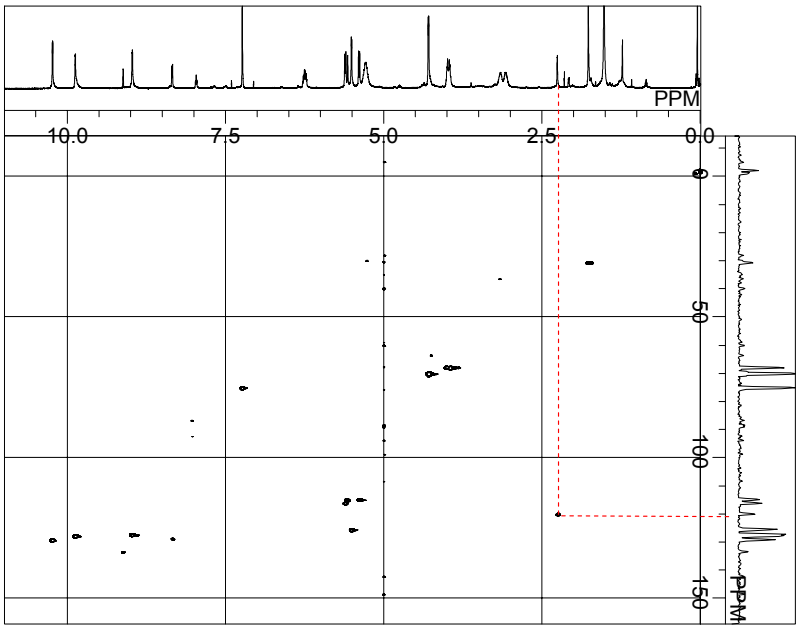

Figure 3.4. HMQC spectrum of **N-EP5** in $CDCl_3$ at room temperature. The proton resonance of Im_4 (2.26 ppm) is correlated with its ^{13}C-signal at 120 ppm.

Moreover, the appearance of β-peripheral protons (β_1) at 5.52 ppm for the macrorings strongly suggests that all the imidazolylporphyrinatozinc(II) in **N-EP5** and **N-EP6** formed a slipped-cofacial dimer and ensures the absence of any noncyclic structures. This was supported by 2D NMR experiments (^{1}H-^{1}H COSY and HMQC) in Figures 3.3 and 3.4. The simplicity of spectra C and D in Figure 3.2 suggests that all ten or twelve porphyrins are identical under the NMR conditions. Thus, inner and outer protons of the macrocyclic arrays could not be discriminated.

The chemical shifts of the phenylene protons H_a and H_c in **N-EP5** and **N-EP6** are sensitive to the spatial positions of the neighboring porphyrins. The slightly larger downfield shift of H_c (9.12 ppm) observed in **N-EP5** relative to that of **N-EP6** (9.07 ppm) can be ascribed to the stronger deshielding effect due to the smaller angle of the pentagonal structure of **N-EP5**. On the other hand, proton H_a in **N-EP5** appears at a slightly upfield position (8.35 ppm) compared to 8.38 ppm for **N-EP6**. The shift behaviors of H_c and H_a protons are reasonably understandable on the basis of the pentagonal and hexagonal geometries. Thus, the NMR data fit nicely to the assumption that **N-EP5** and **N-EP6** adopt distinguishable macrocyclic structures.

It is noteworthy that the observed spectra in Figure 3.2 (C and D) are in sharp contrast to those of macrocyclic porphyrin arrays of zinc-imidazolylporphyrins connected by

sterically hindered spacers.[8b] In the latter case, the inner and outer protons of the macrocyclic arrays in the barrel form were discriminated because the inner protons were more shielded by the ring current effect of nearby porphyrins. Topological isomers were also observed with respect to the coordination manner, indicating a slow exchange rate, if any, among the isomers. In contrast, the porphyrin dimer uints in **N-EP5** and **N-EP6** are conformationally flexible and undergo fast rotation around the ethyne axis on the NMR time scale. If rotation is assumed, the barrier to rotation is presumably small since no noticeable changes in the NMR spectrum were observed at -50°C (Figure 3.5).

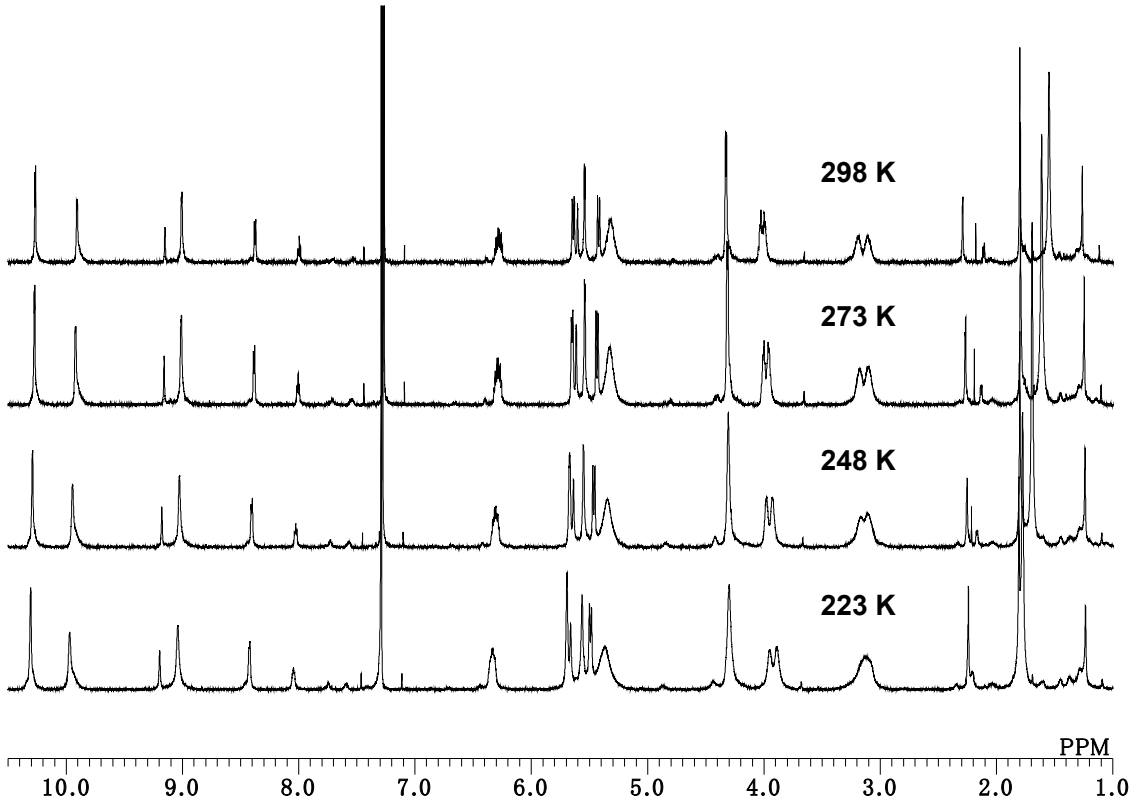

Figure 3.5. Variable-temperature ^{1}H NMR spectra of **N-EP5** in $CDCl_3$.

3.3- STM visualization. The most reliable evidence supporting the formation of macroring was provided by the direct observation of its molecular shape by high-resolution scanning tunneling microscopy (HRSTM). **N-EP5** and **N-EP6** have not been used for the STM observation because the adsorption energy during deposition on STM surface tends to dissociate the self-assembled structure formed in solution. Covalent linking of the coordination pairs was found to be effective in reinforcing the macrocyclic structure on metal surface.[17] Accordingly, the coordination-assembled rings reinforced with covalent linkage, **C-EP5** and **C-EP6**, are expected to survive during deposition on metal surface and to be applicable to STM measurements. Owing to the poor solubility of **C-EP6** in $CHCl_3$,[15] a **C-EP5**-rich sample containing ~2% of **C-EP6** was employed for the measurements.[18] A chloroform solution of the sample (1-0.1 μM) was deposited on a Au (111) surface by the pulse injection technique reported previously.[19]

Images of almost perfect circular shapes composed of five and six bright spots were observed at high bias voltage, Figure 3.6(a). By contrast, STM image at low bias voltage (+2 V) (Figure 3.6(b)) reveals that some rings contain different numbers of bright spots at random. The bright spots are thought to lie at higher position than the other ring components, thus, different brightnesses in this image reflect mainly height of

the moieties. Consequently, the detailed molecular structure at submolecular resolution is obtained by STM at Vs = +2 V.

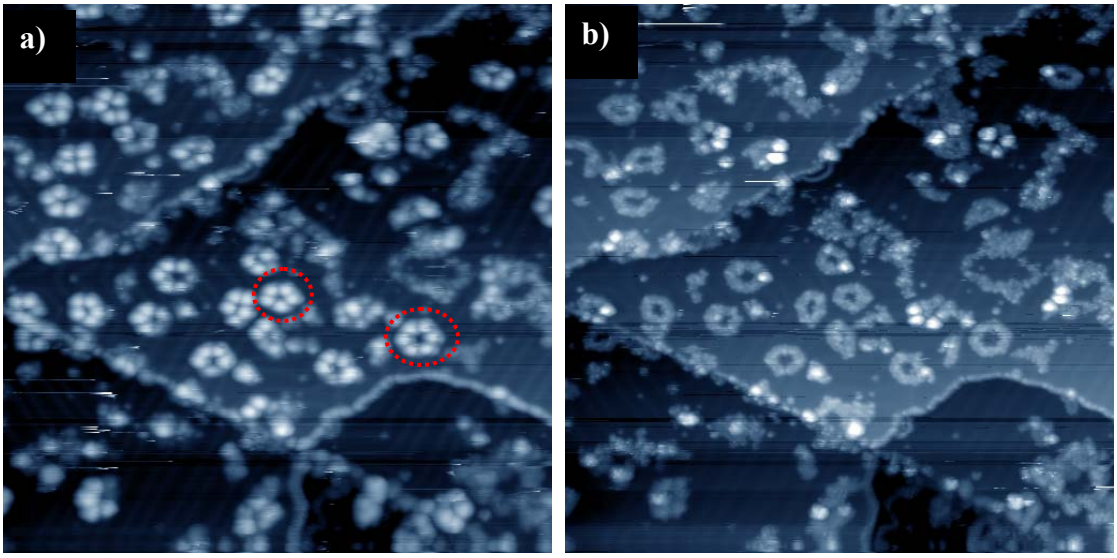

Figure 3.6. HRSTM images of **C-EP5** and **C-EP6** on Au(111). Bias voltage: (a) +4 V, and (b) +2 V. Scale: X = 100 nm.

In order to find the origin of height differences in Figure 3.6(b), two extreme pentagonal rings are magnified as shown in Figure 3.7. Figure 3.7 (a) represents a perfect **C-EP5** ring which appeared as five bright spots of even brightness. The height of each bright spot reaches ca. 6 Å, and the ring size is almost consistent with a molecular model of **C-EP5**, as superimposed in Figure 3.7 (c). The center-to-center distance between two bright spots in the ring (3.6 nm) agrees well with that obtained from the model (3.66 nm). On the other hand, the size of the ring in Figure 3.7 (b) is larger than the model of **C-EP5** and distorted from the symmetric pentagon. An almost flat structure is observed

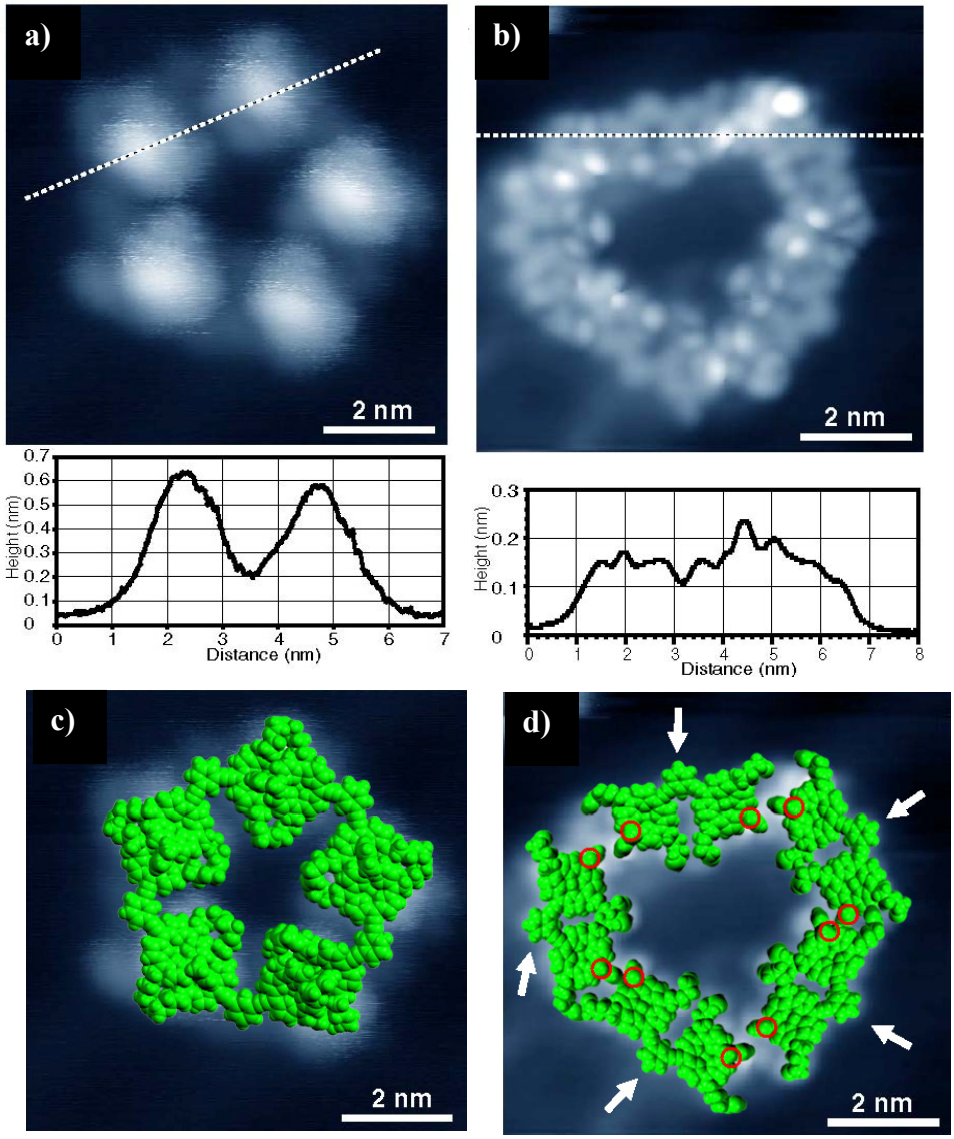

Figure 3.7. Magnified HRSTM images of **C-EP5** on Au(111). (Bias voltage = +2 V, scale: X = 9 nm). (a) Non-disconnected pentameric ring, (b) completely disconnected pentameric ring. Each profile along the dotted line indicated in (a) and (b) is shown below. (c) Superimposed image of molecular model **C-EP5** (green) on (a), and (d) superimposed image of molecular model from five **Zn-EP-Zn** (green) on (b). Red circles in (d) indicate *N*-methyl imidazole parts standing orthogonally to porphyrin planes. They correspond to five pairs of bright spots in (b). White arrows in (d) indicate 1,3-bis(ethynylphenylene) moieties.

in this image, except for one bright dot. The height of the flat part (ca. 1.5 Å) suggested a porphyrin monolayer and the bright dot is higher than the flat part by ~1 Å. STM images obtained at submolecular resolution can be assigned by applying the molecular model of **Zn-EP-Zn** to the images. In this model, two square-shape porphyrins are connected by 1,3-bisethynylphenylene linker with approximately 110° angle. When superimposed images of **Zn-EP-Zn** are applied to Figure 3.7 (b), the characteristic points in the image are assigned as the followings. (1) Five elbows are assigned as 1,3-bis(ethynylphenylene) moieties, as indicated by arrows in Figure 3.7 (d). (2) Square shapes connected to the elbows are assigned as porphyrin rings. (3) Bright dots at the opposite corner to the elbows are assigned as *N*-methyl groups of imidazolyl substituents (red circles in Figure 3.7 (d)) which are higher than porphyrin plane due to their perpendicular orientation. (4) Dots extended from the other two corners are assigned as substituents at the *meso* position of the porphyrins. A completely disassociated hexameric ring (**C-EP6**) was assigned in a similar manner, Figure 3.8.

To confirm the assignment of the ring images in Figures 3.7 and 3.8, STM images of acyclic **C-EP2** are measured at Vs = +2 V, Figure 3.9. Similarly to the ring images, the bright spots observed in the latter image are assigned as the slipped-cofacial dimer moieties.

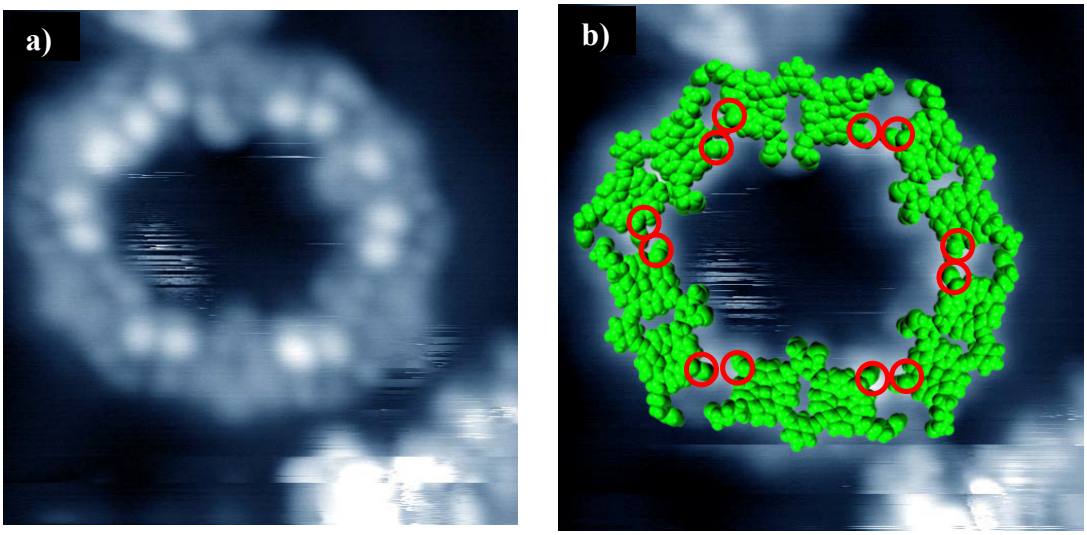

Figure 3.8. HRSTM images of **C-EP6** on Au(111). (Bias voltage = -2 V, scale: X = 9 nm). (a) Completely disconnected hexameric ring, (b) superimposed image of six molecular models of **Zn-EP-Zn** (green) on (a). Red circles in (b) indicate *N*-methyl imidazole parts standing orthogonally to porphyrin planes. They correspond to six pairs of bright spots in (a).

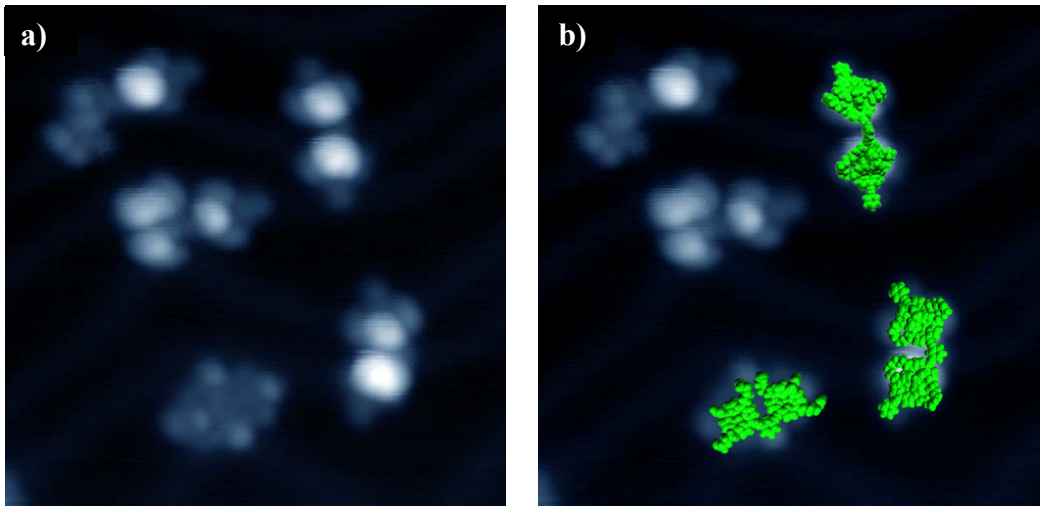

Figure 3.9. HRSTM images of **C-EP2** on Au(111). (Bias voltage = +2 V, scale: X = 20 nm). (b) Superimposed image of molecular model **C-EP2** (green) on (a).

The distance between two bright spots is consistent with that obtained from the molecular model (3.6 nm). Thus, the image of the reference **C-EP2** indicates that non-disconnected slipped-cofacial dimer appears as one bright spot with the height of the dimer. To validate the assignment further, slipped-cofacial dimers were attempted to be disassociated operationally by repeated scanning of a non-disconnected **C-EP6** ring. As can be seen in Figures 3.10 (a) and (b), the intact hexameric ring appears as six bright spots corresponding to six slipped-cofacial dimers. One of the bright spots darkened after the eighth scanning (Figure 3.10 (c)), another after the twelfth scanning (Figure 3.10 (d)). These results indicate that scanning triggered disassociation of the dimer. Accordingly, it can be concluded that the disassociated structures (flat structures) originate from the slipped-cofacial dimers.

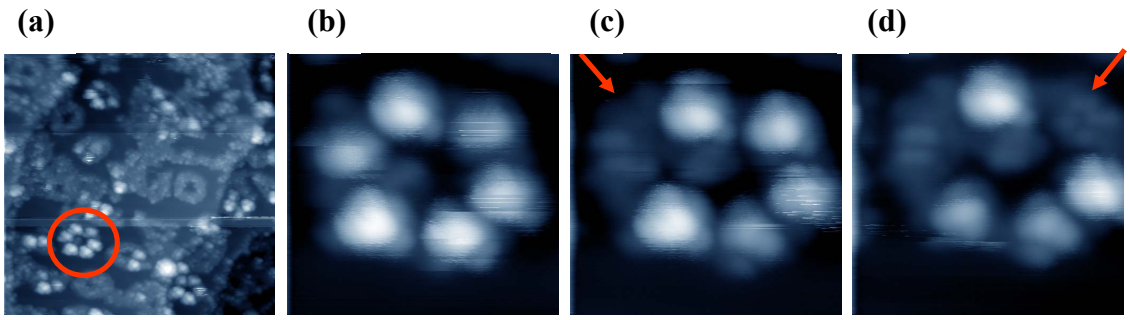

Figure 3.10. Successive HRSTM images of **C-EP6** on Au(111). (Bias voltage = +2 V). Scale: (a) X = 50 nm, (b), (c) and (d) X = 9 nm. (a) Non-disconnected hexameric ring indicated by a red circle, (b) magnified image of **C-EP6** in (a), the initial state, (c) after 8th scans, (d) 12th scans. Red arrows in (c) and (d) indicate disassociated dimers due to repeated scans.

Besides scanning, molecule-metal surface interaction contributes to structure disassociation on STM surface. The adsorption energy generated from the deposition process is thought to be enough to dissociate the complementary coordination and covalent bonds of the slipped-cofacial dimer. After the dissociation, lateral intermolecular interactions (e.g. van der Waals interaction) become dominant and give flat and closely packed ring structure. This structure is the most stable form on gold surface given the fact that most of the rings in STM images appeared flat. In solution, since the macroring can diffuse and rotate freely, intermolecular interactions work into any direction to give three-dimensional macrocyclic architecture, as evidenced by ^{1}H NMR. On STM surface, however, the intermolecular interactions are restricted to lateral direction of the adsorbed molecule. Therefore, the most stable structure in solution is inconsistent from that on metal surface.

In a previous report on STM observation of ferrocence-bridged trisporphyrin macrorings,[17] although the numbers of aggregated units were resolved clearly, submolecular resolution was not achieved as in the present case. The above observations of **C-EP5** and **C-EP6** are considered a rare example of complex macroporphyrin images. The resolution reached a submolecular level, representing one of the best resolved STM images of molecules of the dimension larger than 5 nm. [20]

3.4- Experimental section for STM measurement

General procedure. The substrate was a Au(111) surface, cleaned to be atomically flat by Ar ion sputtering at a high temperature of 500 °C in high vacuum. A chloroform solution of the sample (1~0.1 μM) was deposited on Au (111) surface by the pulse injection technique reported previously.[19] The deposition temperature was room temperature. The prepared samples were transferred to the observation chamber of an STM stage in an ultrahigh vacuum of better than 10^{-8} Pa. The STM chamber was cooled by liquid nitrogen; the observation temperature was 80 K. The STM system was an LT-STM (Omicron, Germany). The tip used was a Pt-Ir tip, and it was sharpened by the electric pulse in the main chamber before the observation. The feed back system is operated at the constant-current mode with a tunneling current of either 4 or 10 pA. The scanning rate was between 0.5 and 2 Hz, with 512 lines per frame.

Chapter 4- Photophysical Characterization of the Macrorings

4.1- Steady-state absorption measurement. The electronic ground-state absorption spectra of the macrorings and reference porphyrins were measured in toluene and pyridine. In both solvents the UV-vis absorption characteristics of the porphyrin macrorings and references are typical to those of *meso*-alkynyl substituted porphyrins namely, the red-shifted absorption spectra and the intensified Q-band (S_0-S_1) relative to the Soret band (S_0-S_2).[21] The spectra of the self-assembled macrorings (**N-EP5** and **N-EP6**) and a reference porphyrin (**Zn-EP**) in toluene are shown in Figure 4.1. Under these conditions, zinc-imidazolylporphyrin exists solely as a dimeric form. The most notable observation in Figure 4.1, is that the spectra of **N-EP5** and **N-EP6** are red-shifted by 337 cm^{-1} and 432 cm^{-1}, respectively, (at low energy Soret band) relative to that of the constituent dimer unit (**Zn-EP** dimer). The Q(0,0) band of **N-EP5** and **N-EP6** is also red-shifted by 164 cm^{-1} and 176 cm^{-1}, respectively, and intensified as compared to that of **Zn-EP** dimer. These spectral changes are indicative of substantive interactions among the constituent porphyrins in the macrorings via exciton coupling mediated by the aryl bisethyne linker. More red shifts exhibited by the hexameric ring relative to the pentameric one implying an increase in the electronic communications in the hexameric ring.

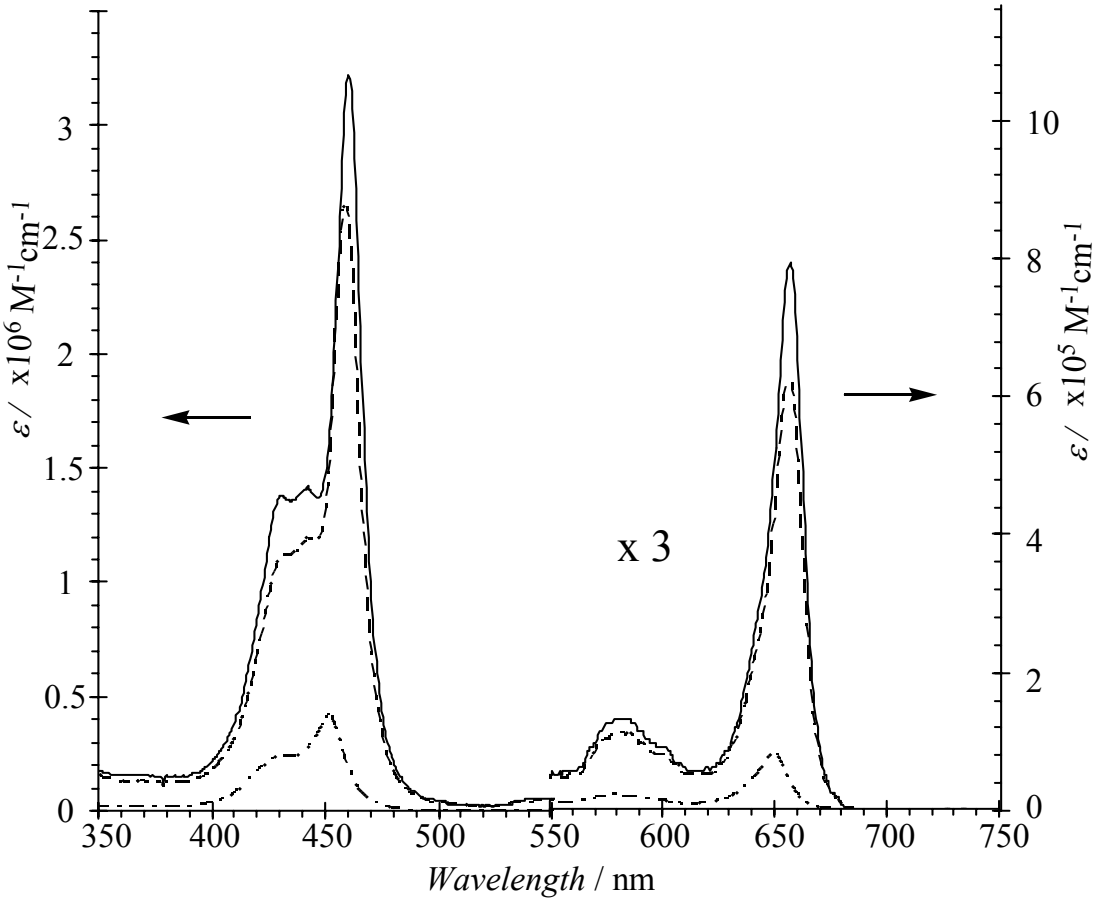

Figure 4.1. Steady-state absorption spectra of **N-EP6**, **N-EP5** and **Zn-EP** dimer (from top to bottom) in toluene at room temperature.

To gain further insight into the nature of dipole interactions in the macrorings and assess the effect of the linker on ground-state absorption spectra, the absorption spectra of series of cyclic and non-cyclic porphyrins connected by phenylethynyl- and phenyl-linkers were measured and compared in pyridine.

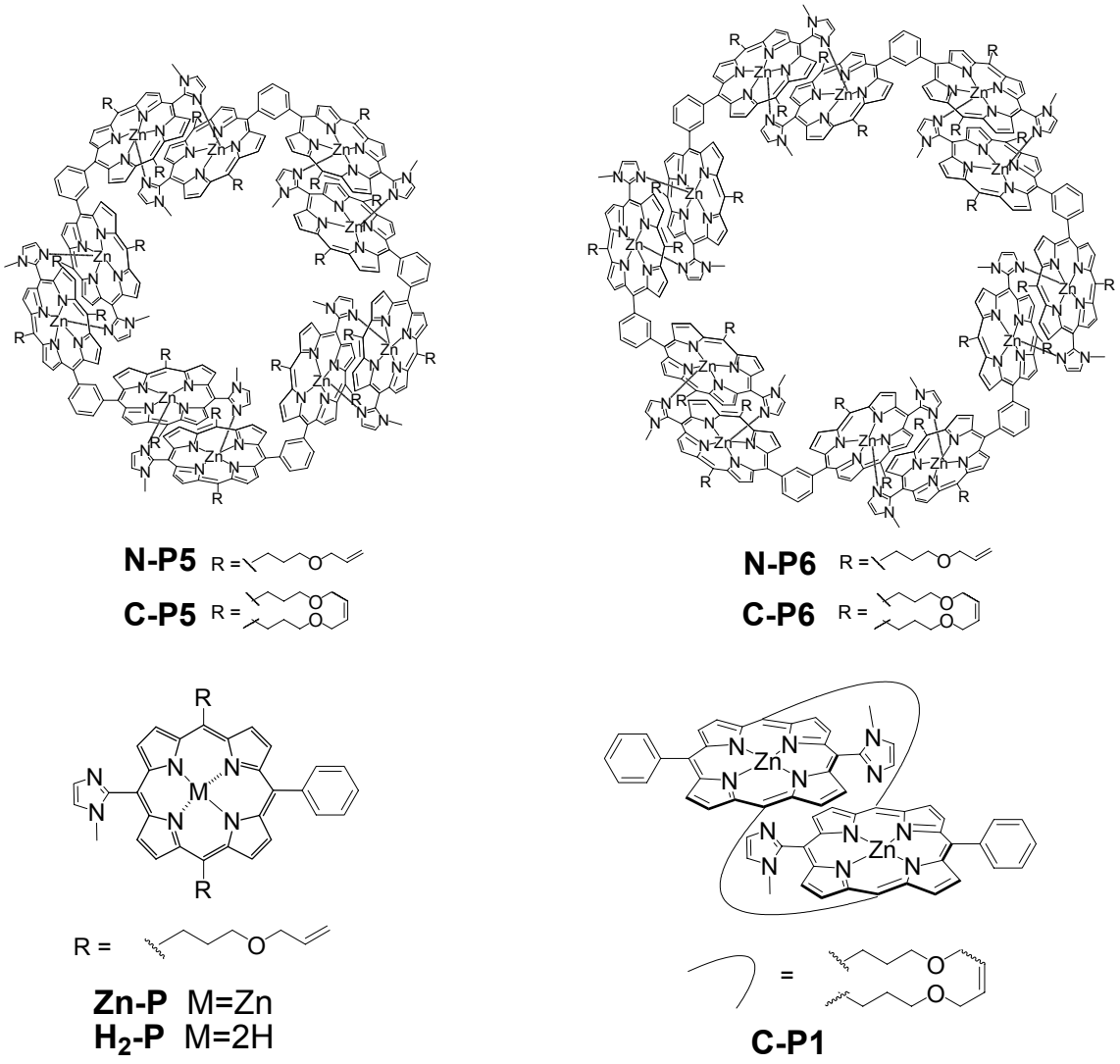

Figure 4.2. Structures of cyclic and non-cyclic phenylene-linked porphyrin references.

The structures of cyclic and non-cyclic phenylene-linked porphyrin references are shown in Figure 4.2. Detailed studies on syntheses and photophysical properties of these references were reported elsewhere in the literatures.[8a,e,10]

Because of the poor solubility of **C-EP6** in other common solvents,[15] pyridine was chosen to compare the whole series of cyclic and non-cyclic porphyrins.

Unlike toluene, pyridine dissociates the non-covalently linked dimers into monomeric species, and the absorption spectra of **Zn-EP** and **Zn-P** in pyridine represent the corresponding monomeric species with axial pyridyl coordination. In contrast, the covalently linked arrays **C-EP1**, **C-EP2**, **C-P1**, **C-EP5**, and **C-EP6** maintain their complementary coordinated structures in pyridine. Figure 4.3 compares the absorption spectra of **Zn-EP**, **C-EP1**, **Zn-P**, and **C-P1** in pyridine.

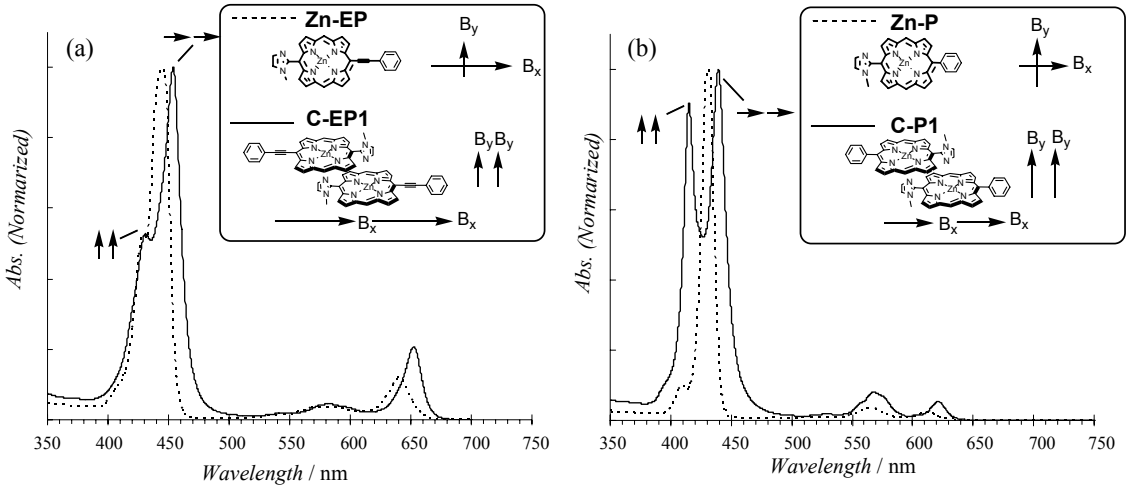

Figure 4.3. UV-vis absorption spectra of (a) **Zn-EP** (dashed line) and **C-EP1** (solid line) and (b) **Zn-P** (dashed line) and **C-P1** (solid line) in pyridine at room temperature. Inset: schematic dipole directions and dipole-dipole coupling.

In monomeric **Zn-P**, the two transition diploes B_x and B_y in the porphyrin plane are degenerate to show one strong Soret band at 431.8 nm. By contrast, monomeric **Zn-EP**

shows two Soret bands at 433.6 and 445.8 nm due to the presence of nondegenerate B_x and B_y transition dipoles. The absorption intensity of B_x at the longer wavelength B_x (445.8 nm) is much larger.

A *meso*-ethynyl group provides a strong effect to porphyrin π-conjugated ring, and the conjugation is well expanded over the phenylethynyl substituent, resulting in the removal of the degeneracy of the porphyrin e_g LUMO orbital. This effects the *x*- and *y*-polarized transitions inequivalent and intensifies the quasi-allowed Q-band by intensity-borrowing from the Soret-transitions.[22] Consequently, the transition dipoles of **Zn-EP** are nondegenerate and the relative intensity of its Q(0,0) band increases as compared to that of **Zn-P**. When the dimer (**C-EP1**) is formed, only the lower energy Soret band is red-shifted by 7.8 nm, whereas the higher energy band remains at the same wavelength. This behavior sharply contrasts with that shown by **C-P1**, in which the degenerate Soret band (431.8 nm) splits into two bands at 415.8 and 440.0 nm due to excitonic dipole-dipole coupling by slipped-cofacial coordination as indicated in Figure 4.3 (b). The negligible blue-shift in the case of **C-EP1** may reflect the small oscillator strength of B_y.[23]

Figure 4.4 shows the steady-state absorption spectra of **Zn-EP-Zn**, **C-EP1**, **C-EP2**, **C-EP5**, and **C-EP6** recorded in pyridine at ambient temperature. The molar extinction

coefficients (ε) of the series **C-EP1**-**C-EP6** are approximately proportional to the increasing number of dimer units. In other words, each dimer moiety in the array can act as independent light absorbing unit. The absorption spectrum of **Zn-EP-Zn** shows a broad Soret band caused by through-space excitonic coupling between two porphyrin units via the linker. In the case of **C-EP2**, which has two cofacial dimers, three Soret bands were observed at 431, 450, and 458.5 nm. The split bands (450 and 458.5 nm) can be ascribed to the dipole-dipole interaction between two adjacent dimers as shown in Figure 4.5.

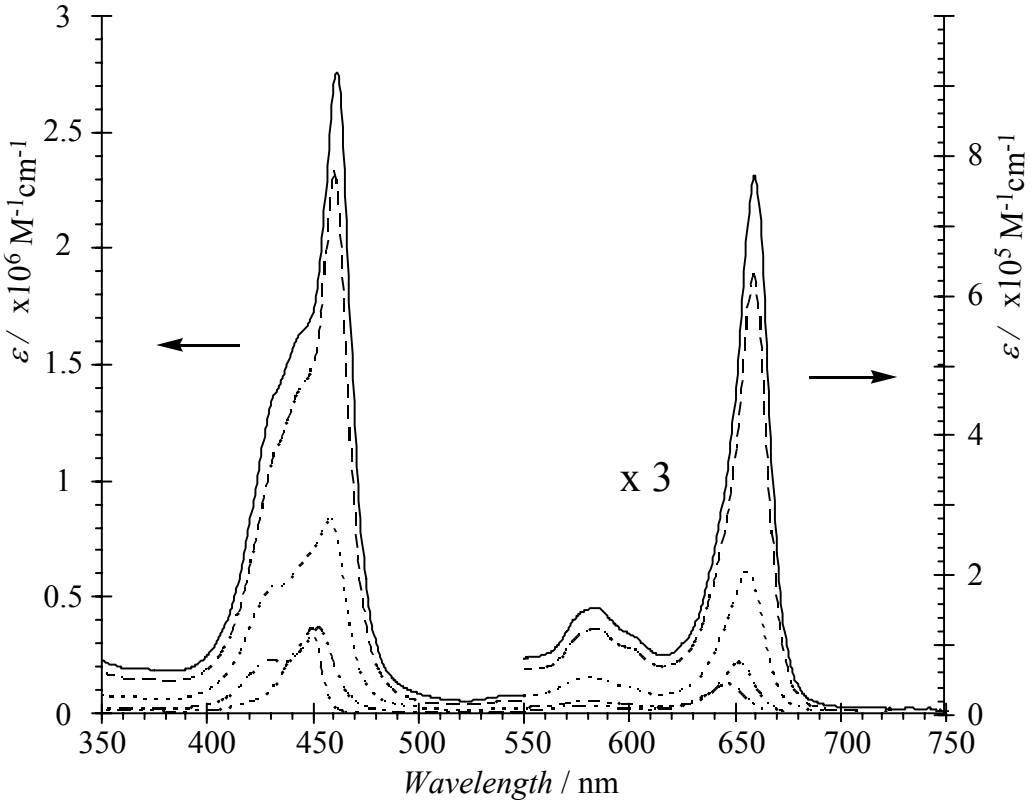

Figure 4.4. UV-vis absorption spectra of **Zn-EP-Zn**, **C-EP1**, **C-EP2**, **C-EP5**, and **C-EP6** (from bottom to top) in pyridine at room temperature.

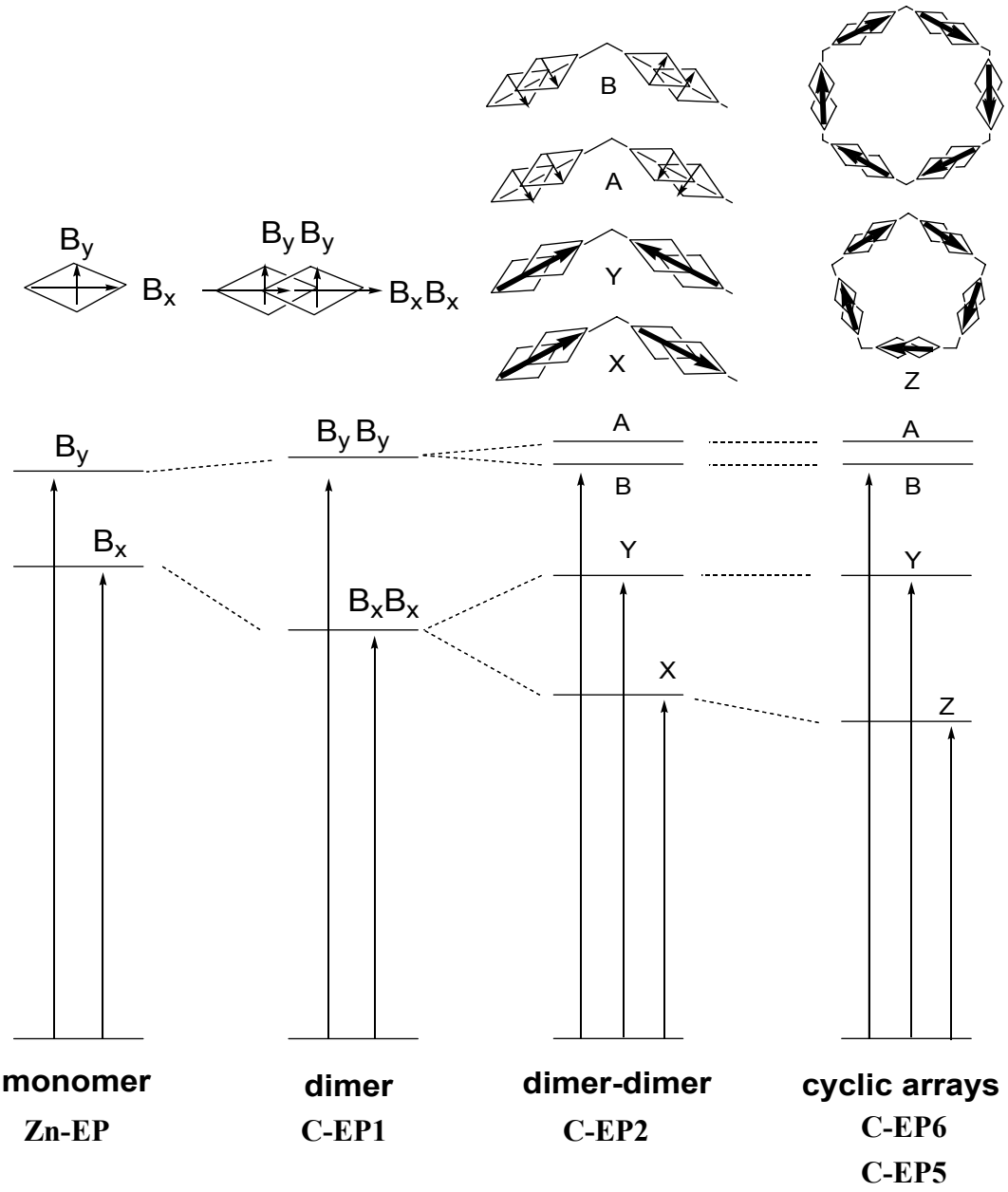

Figure 4.5. Exciton coupling at the Soret bands of **Zn-EP**, **C-EP1**, **C-EP2**, **C-EP5**, and **C-EP6**.

Thus, the interaction between two dipoles of two dimers produces the new integrated dipoles X (red-shift) and Y (blue-shift). The lowest energy Soret band and the Q(0,0) band are red-shifted considerably by the interaction. Further red shifts of these bands are observed in the case of the macrocyclic arrays **C-EP5** and **C-EP6** due to the interaction with two adjacent dimers. An interesting feature in Figure 4.4, is that the absorption spectra of **C-EP5** and **C-EP6** exhibit sharper Soret bands relative to those of **C-EP1** and **C-EP2**, presumably reflecting the structural flexibility in solution of **C-EP1** and **C-EP2** and the relative rigidity of **C-EP5** and **C-EP6** through cyclic formation.

Further details on the absorption peaks of Soret– and Q-bands of the investigated porphyrin series can be found in Table 1.

4.2- Steady-state fluorescence measurement. The steady-state fluorescence spectra of **C-EP1**, **C-EP2**, **C-EP5**, and **C-EP6** are shown in Figure 4.6, and their emission peak maxima, Stokes shifts, and quantum yields relative to ZnTPP (Φ_F = 0.038 in pyridine) are listed in Table 1. The fluorescence spectra were red-shifted in going from **C-EP1** and **C-EP2** to **C-EP5** and **C-EP6**, in line with their Q-band tail positions. The linear series (**C-EP1** and **C-EP2**) exhibit larger Stocks shifts as compared to those of the cyclic series (**C-EP5** and **C-EP6**). This reflects larger structural changes between excited and ground states of the linear series, which is again consistent with their

absorption spectra exhibiting larger inhomogenous broadening. The fluorescence quantum yield of **C-EP1** (9.3%) is slightly higher than that of **Zn-EP** (8.3%), and its Stocks shift is smaller (112 cm^{-1} for **C-EP1** and 235 cm^{-1} for **Zn-EP**), indicating that the dimer provides a more rigid structure and raises the fluorescence intensity compared to **Zn-EP**. In general, increasing the aggregation number tends to induce the formation of an energy sink, where the singlet excitation energy is lost through internal conversion to vibrational states, thereby decreasing the fluorescence quantum yield.

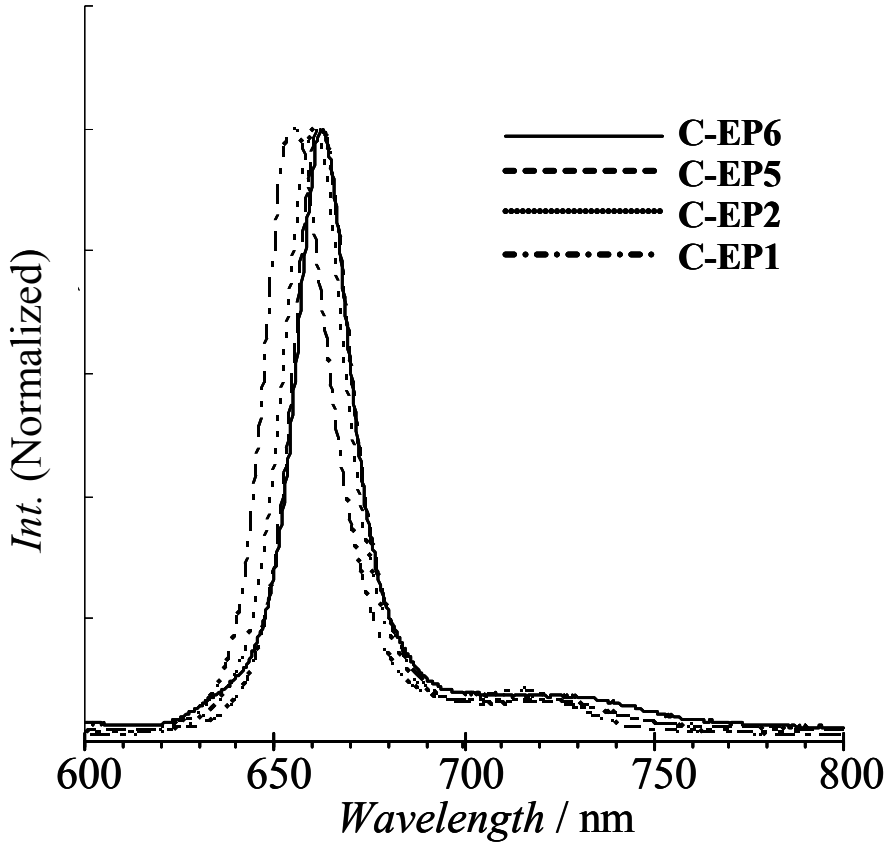

Figure 4.6. Normalized fluorescence spectra of **C-EP1**, **C-EP2**, **C-EP5**, and **C-EP6** taken for excitation at 430 nm in pyridine.

In the present case, however, the increase in the number of dimer units (two for **C-EP2**, five for **C-EP5**, and six for **C-EP6**) does not quench the fluorescence and the quantum yield increases along with increasing the number of dimer units. Thus, perfectly satisfying an important functional prerequisite for LH antennae. Because of the inherently high fluorescence quantum yield of **Zn-EP** (8.3%), as compared with those of zinc (II) porphyrin substituted by *meso*-tetraaryl and alkyl groups (normally Φ_F = 3-4%), macrocyclic **C-EP5** and **C-EP6** exhibit the highest class of fluorescence quantum yields as porphyrin arrays.

4.3- Fluorescence lifetime. The time-resolved fluorescence decays were measured at several wavelengths in pyridine by a time-correlated single-photon-counting (TCSPC) technique at the magic angle, and their fitted parameters are summarized in Table 1. The λ_{ex} = 420 nm and λ_{em} = 650 nm were applied for the isotropic fluorescence measurements and the fluorescence lifetimes were obtained by averaging the fitted parameters measured in several emission wavelengths (Figure 4.7). The fluorescence decays do not show any emission wavelength dependence, implying single-exponential relaxations from the lowest singlet S_1 states of porphyrins. The fitted S_1 state lifetimes are shortened slightly in the order **C-EP1** > **C-EP2** > **C-EP5** > **C-EP6**. The steady-state fluorescence quantum yields increase in the same order. Therefore, these results indicate

that the radiative decay rate k_F increases relative to the other decay rates as the number of ring components increases. The Stocks shifts also decrease slightly from 92 cm^{-1} (**C-EP5**) to 88 cm^{-1} (**C-EP6**), indicating that the structural difference between ground and excited states decreases by forming rigid cyclic pentamers and hexamers. This trend is more evident in the non-covalently linked rings (**N-EP5** and **N-EP6**) in toluene. The faster k_F and smaller Stocks shift of **EP6** seem to be correlated.

Table 1. Absorption and fluorescence spectral data

Sample	Solvent[a]	Absorption Soret/nm			Q(0,0) /nm	Fluorescence Q(0,0) emission[b] λ_{max}/nm	Stokes shift /cm^{-1}	Quantum yield[b, c] Φ_F	Lifetime[d] τ/ns
Zn-EP	Py	433.6	-	445.8	640.6	650.4	235	0.083	-
C-EP1	Py	433.6	-	453.6	651.8	656.6	112	0.093	1.65
Zn-EP-Zn	Py			450.2	646.8	653.4	156	0.100	-
C-EP2	Py	431	450	458.5	656.5	660.8	99	0.100	1.45
C-EP5	Py	431	443	460.6	659.0	663.0	92	0.101	1.42
C-EP6	Py	431	443	461.4	659.4	663.2	88	0.110	1.38
Zn-P	Py	-	431.8	-	612.4	-	-	-	-
C-P1	Py	415.8	-	440.0	621.8	-	-	-	-
C-P5[e]	Py	410	425	447	621	626.5		0.035[f]	2.18
C-P6[e]	Py	410	425	449	622	627		0.035[f]	2.19
Zn-EP[g]	Tol	433.5	-	451.5	649.5	654.8	124.6	0.093	-
C-EP2	Tol	433.5	-	458.5	655	658.8	88	0.095	-
N-EP5	Tol	431.5	442.5	459.0	656.5	659.2	62.4	0.095	-
N-EP6	Tol	431	442	460.5	657	659.4	55	0.100	-

[a] Py: pyridine, Tol: toluene. [b] Excited at 430 nm. [c] ZnTPP in pyridine (Φ_F =0.038) was used as reference. [d] λ_{ex} = 420 nm and λ_{em} = 650 nm were applied. [e] [ref. 10]. [f] Data for **N-P5** and **N-P6** in toluene [ref. 8f]. [g] Coordination dimer is formed.

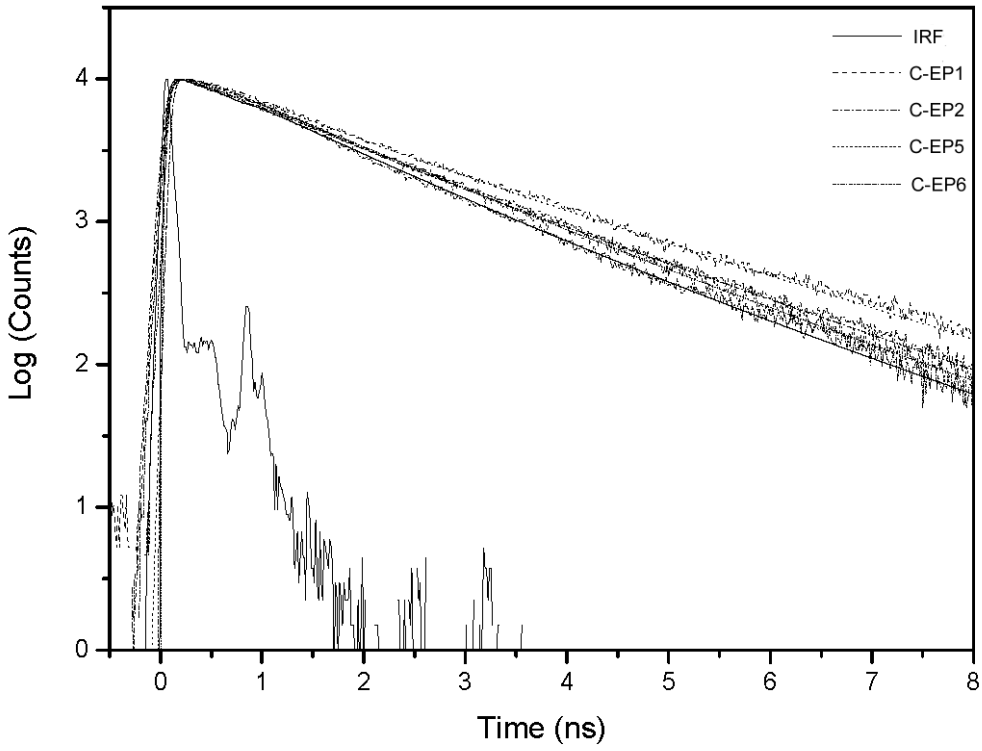

Figure 4.7. Time-resolved fluorescence decay profiles of **C-EP1**, **C-EP2**, **C-EP5**, and **C-EP6** in pyridine, where the excitation and the emission wavelengths were 420 and 650 nm, respectively. Instrumental response function (IRF) of the TCSPC system was ~60 ps.

4.4- Fluorescence excitation anisotropy. The steady-state fluorescence excitation anisotropy (FEA) spectra in pyridine were recorded at 670 nm to obtain information on the relative orientation between absorption and emission transition dipole moments (Figure 4.8). The maxima and minima anisotropy values around the Soret bands are tabulated in Table 2. The steady-state FEA spectra showed negative anisotropy values (r) in the high energy Soret band and positive values at both low energy Soret and Q-bands for all four molecular systems.[10] It is to be noted that the absolute r values

were smaller in **C-EP5** and **C-EP6** compared to **C-EP1** and **C-EP2**, indicating the existence of additional depolarization channels in the cyclic assembly systems. On the assumption that the magnitudes of *r* values originate mainly from the depolarization processes by the rotational diffusion motion in solution, the cyclic molecular systems should have larger *r* values than those of the linear references **C-EP1** and **C-EP2** because of their larger hydrodynamic volumes.[24] Thus, the relatively small *r* values in cyclic systems should originate from another depolarization channel, such as the redistribution of transition dipoles by the excitation energy hopping process.[25]

4.5- Fluorescence anisotropy decay. The fluorescence anisotropy decay profiles of **C-EP1**, **C-EP2**, **C-EP5**, and **C-EP6** were also measured (Figure 4.9), for which the λ_{ex} = 420 nm and λ_{em} = 650 nm were employed. The fitted decay parameters are listed in Table 2. The fluorescence anisotropy decays of **C-EP1** and **C-EP2** were fitted with the time constants of 1.07 and 2.73 ns, respectively, representing the rotational correlation times. In the case of **C-EP5** and **C-EP6**, on the other hand, the temporal profiles were fitted with the biexponential function, which showed a time constant of less than ~40 ps and much longer (> 10 ns).

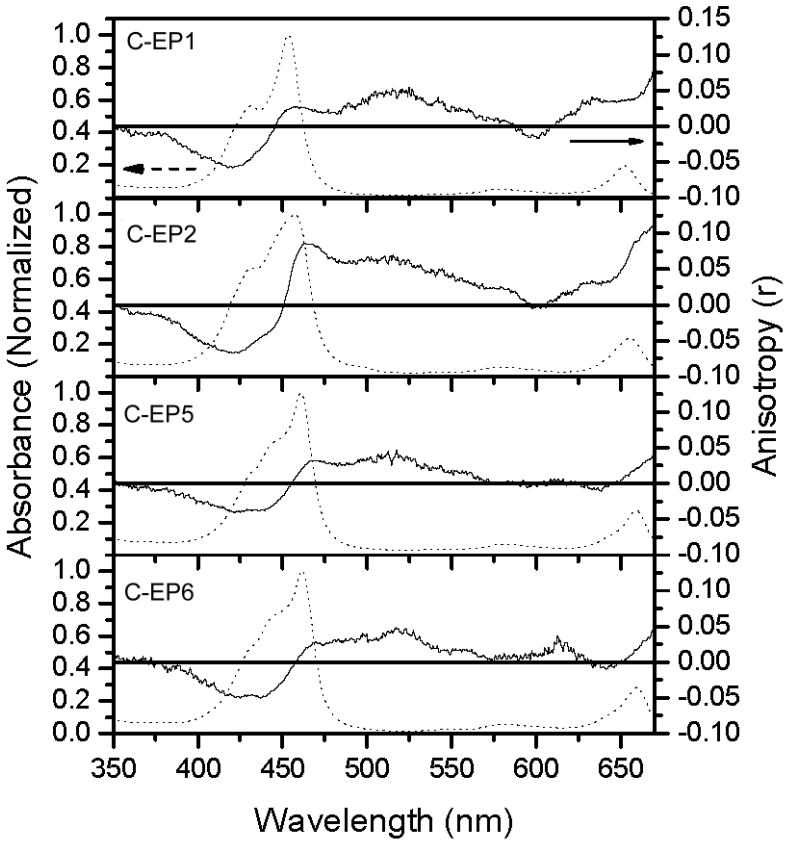

Figure 4.8. Steady-state fluorescence excitation anisotropy spectra of **C-EP1**, **C-EP2**, **C-EP5**, and **C-EP6** in pyridine recorded at 670 nm. The polarized excitation spectra (I_{VV} and I_{VH}) were measured and calculated by $r = (I_{VV} - GI_{VH})/ (I_{VV} + 2GI_{VH})$.

Table 2. Fluorescence excitation anisotropy (r) and anisotropy decay time (Φ)[a]

Sample	r_{max}[b]	r_{min}[c]	Φ[d]/ns
C-EP1	0.04	-0.06	1.03
C-EP2	0.09	-0.07	2.73
C-EP5	0.03	-0.04	-
C-EP6	0.03	-0.05	-

[a] All the experiments were performed in pyridine. [b, c] The maxima and minima anisotropy values around Soret bands (Figure 4.8). [d] The λ_{ex} = 420 nm and λ_{em} = 650 nm were applied for the anisotropic fluorescence measurement (Figure 4.9). The anisotropy decay times were obtained by averaging the fitted parameters measured in several emission wavelengths.

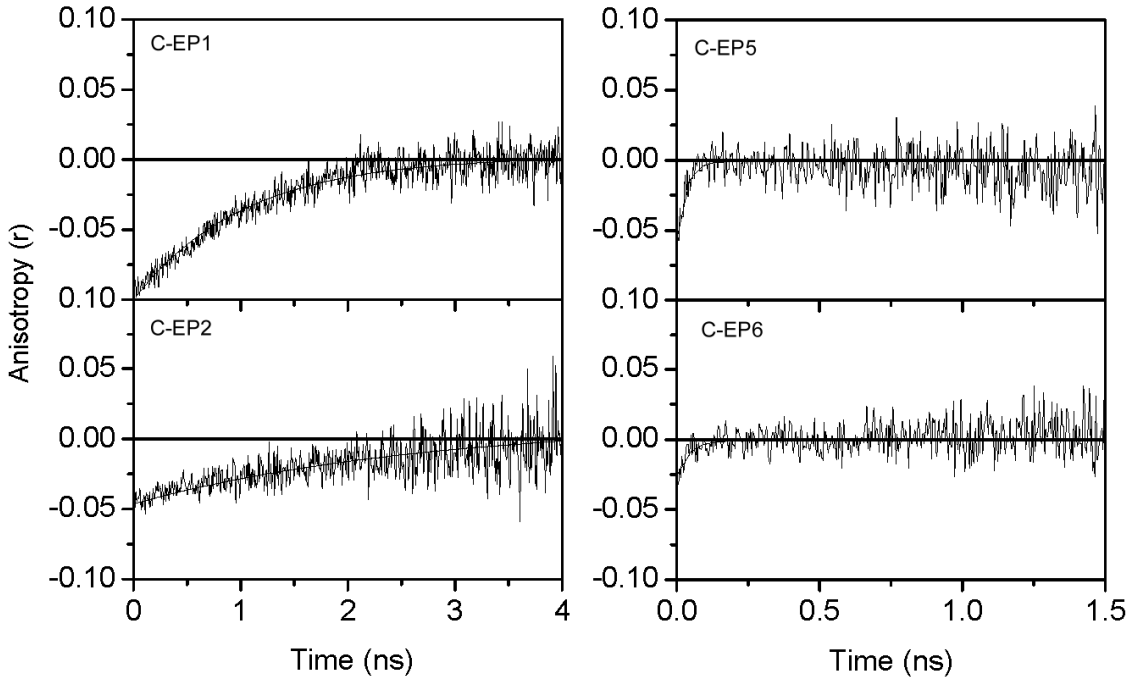

Figure 4.9. Time-resolved fluorescence anisotropy decay profiles of **C-EP1**, **C-EP2**, **C-EP5**, and **C-EP6** in pyridine, where the excitation and the emission wavelengths were the same as those of the experiment of magic angle fluorescence decay. The polarized excitation spectra (I_{VV} and I_{VH}) were measured, and the time-resolved anisotropy decay $r(t)$ was calculated by $r(t) = \{I_{VV}(t) - GI_{VH}(t)\}/\{I_{VV}(t) + 2GI_{VH}(t)\}$.

Because of the large hydrodynamic volumes of **C-EP5** and **C-EP6**, the fast depolarization component (~40 ps) could not be assigned to rotational diffusion processes. Instead, it was assigned to other depolarization channels, such as energy migration or transition dipole redistribution processes. As a result, the EEH processes in **C-EP5** and **C-EP6** were assumed to occur in a few tens of picoseconds.

4.6- Isotropic and anisotropic transient absorption measurement. To investigate the EEH processes along the cyclic arrays, femtosecond transient absorption (TA) decay with pump power dependence as well as transient absorption anisotropy (TAA) changes were simultaneously measured. The excitation wavelength was tuned for the Q-band (λ_{pump} = 650 nm), because the Q-band excitation could eliminate complicated processes caused by the involvement of internal conversion process from the S_2 to S_1 state.

The transient absorption decays corresponding to the induced absorption signal were measured at the magic angle (Figure 4.10). The fitted parameters and the pump power conditions are summarized in Table 3. As displayed in Figure 4.10, **C-EP1** showed no pump power dependence as the intensity of the pump pulse was varied from high (1.8 mW) to low (0.3 mW). In contrast, when **C-EP2** was excited by high pump power, two fast decay components (0.48 and 14 ps) and a slow decay component (1.45 ns) were observed, though no fast component was observed under low power conditions, where the time constant of the slow decay component (τ_3) was fixed as the S_1 state lifetime as revealed by the fluorescence decay measurements (Table 1). In **C-EP5** and **C-EP6**, one slow and two fast decay components were observed even under low pump power conditions. The amplitudes of the two fast components became dominant under high power conditions, i.e., 58% and 50% for **C-EP5** and **C-EP6**, respectively.

Table 3. Transient absorption decay time constants at magic angle[a] with pump power dependence of **C-EP1**, **C-EP2**, **C-EP5** and **C-EP6** in pyridine.

Sample	Power[b]	τ_1	τ_2	τ_3
C-EP1		-	-	1.65 ns
	1.8 mW	-	-	100%
	0.6 mW	-	-	100%
	0.3 mW	-	-	100%
C-EP2		0.5 ps	14 ps	1.45 ns
	1.8 mW	31%	7%	62%
	0.6 mW	-	-	100%
	0.3 mW	-	-	100%
C-EP5		1.3 ps	22 ps	1.42 ns
	1.8 mW	32%	26%	42%
	0.6 mW	24%	11%	65%
	0.3 mW	43%	3%	54%
C-EP6		2.0 ps	19 ps	1.38 ns
	1.8 mW	29%	21%	50%
	0.6 mW	32%	2%	66%
	0.3 mW	24%	5%	71%

[a] The λ_{pump}= 650 nm and λ_{probe}= 520 nm were applied for the transient absorption measurement. [b] The pump energy per pulse was 360, 120 and 60 nJ for 1.8, 0.6 and 0.3 mW, respectively, because the repetition rate of 5 KHz was applied.

Notably, the amplitudes of the medium component in **C-EP5** (22 ps) and **C-EP6** (19 ps) increased as the pump power increased from 0.3 to 1.8 mW. These time constants were considered to represent the S_1-S_1 exciton-exciton annihilation processes, since they become manifest only under high pump power conditions.

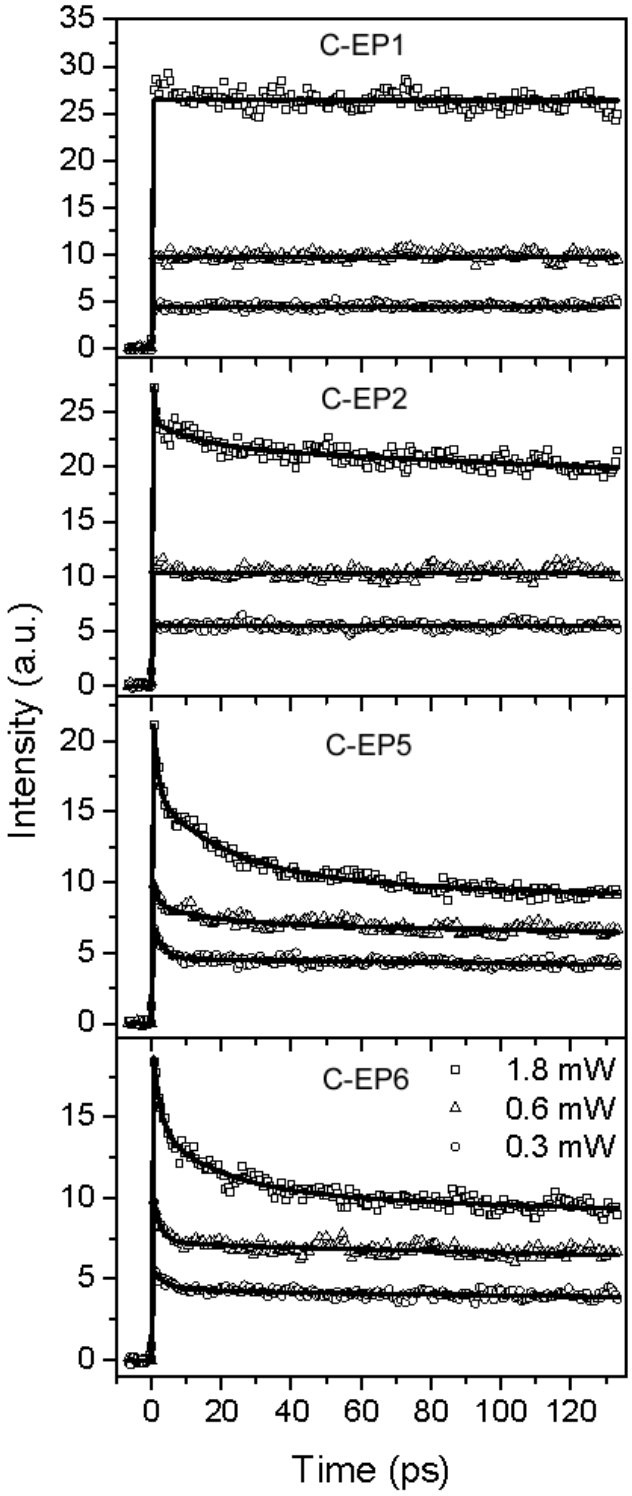

Figure 4.10. Transient absorption decay profiles of **C-EP1**, **C-EP2**, **C-EP5**, and **C-EP6** (from top to bottom) in pyridine including pump power dependence, where the pump and probe wavelengths were 650 and 520 nm, which are the Q-band excitation and induced-absorption probe, respectively.

The pump power dependence on the TA decay is indicative of the exciton-exciton annihilation process, because intense excitation or high density of photons generates two or more excitons in one cyclic array, and then the recombination process between them creates a fast deactivation channel.[26] The fastest components (1-2 ps) observed for **C-EP5** and **C-EP6** are expected to be associated with higher order annihilation processes, which could be observed in multichromophoric systems, especially when the samples are excited by high pump power pulses. Figure 4.10 indicates that the exciton-exciton annihilation of **C-EP5** and **C-EP6** is due to the exciton-exciton recombination between units of **C-EP1** rather than zinc(II)-porphyrin monomers, because this process does not occur in **C-EP1**. According to the previous description on the natural light-harvesting antennae such as LH1 and LH2, the exciton-exciton annihilation process is conceived as a Förster-type incoherent EEH process from the excited donor to the proximal excited acceptor resulting in a doubly excited acceptor state; the latter quickly relaxes to the singly excited state.[26] Therefore, the exciton-exciton annihilation process should be a direct evidence of the Förster-type incoherent EEH process within the cyclic array.

The transient absorption anisotropy (TAA) measurement is also a helpful tool to investigate the excitation energy migration process along the cyclic array, because the

EEH process even between the same molecular units aligned in different direction creates a depolarization channel. The TAA decay profiles (Figure 4.11) were obtained under low pump power conditions to avoid multiexciton processes observed in the power dependence experiments. The fitted parameters are listed in Table 4. In **C-EP1**, the anisotropy decay was fitted with a fast (~300 fs) and a slow (~1 ns) decay component in a short time window (13 ps). The observed fast decay component (~300 fs) was similar to that of the dimer **C-P1** (200 fs). Because the B_x and B_y equilibrium process inside zinc(II)-porphyrin monomers of **C-P1** proceeds on the timescale of ~200 fs, the fast τ_1 component in **C-EP1** (~300 fs) was assigned to both the intrachromophoric dipole equilibrium (dephasing process) and the interchromophoric EEH process within the cofacial dimer.[10] The steady-state absorption spectral shapes of **C-EP1** differ significantly from those of **C-P1** with the introduction of the ethynyl moiety. A much higher oscillator strength was observed for the B_x component (along the ethyne axis) as compared to B_y. The uneven transition dipoles may suppress the exchange rate significantly. In addition, the slow component (~1 ns) is consistent with the anisotropy decay observed in the TCSPC experiment (Table 2) and is assigned to the rotational correlation time.

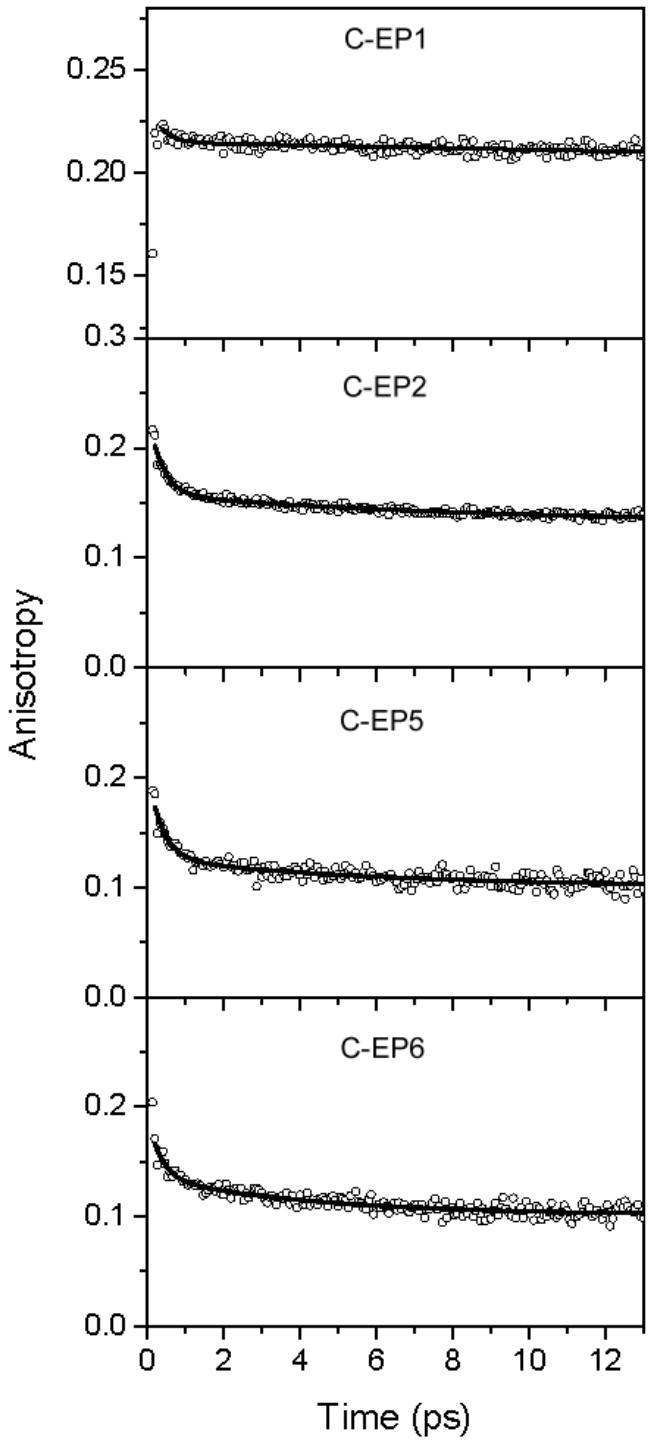

Figure 4.11. Transient absorption anisotropy decay profiles of **C-EP1**, **C-EP2**, **C-EP5**, and **C-EP6** (from top to bottom) in pyridine, where the pump and probe wavelengths were 650 and 520 nm, which are the Q-band excitation and induced-absorption probe, respectively.

Table 4. Transient absorption anisotropy decay time constants of **C-EP1**, **C-EP2**, **C-EP5** and **C-EP6** in pyridine.[a]

Sample	τ_1 (%)	τ_2 (%)	τ_3 (%)	r_∞
C-EP1	0.3 ps (4%)		1.03 ns (96%)	0.20
C-EP2	0.27 ps (35%)	4.3 ps (10%)	2.70 ns (55%)	0.14
C-EP5	0.36 ps (39%)	5.4 ps (13%)	5 ns < (48%)	0.10
C-EP6	0.33 ps (29%)	4.2 ps (18%)	5 ns < (53%)	0.10

[a] The λ_{pump}= 650 nm and λ_{probe}= 520 nm were applied for the measurement. The anisotropy decay profiles were obtained under a low pump power condition (0.3 mW).

In contrast to **C-EP1**, three decay components were observed for **C-EP2**, **C-EP5**, and **C-EP6**. The slowest component in **C-EP2** was fitted to 2.7 ns, which is in accordance with the anisotropy decay observed in TCSPC (Table 2), and those in **C-EP5** and **C-EP6** (>5 ns) could not be assigned exactly but are expected to be associated with the rotational correlation times. Besides the fastest time constant (~300 fs), which could be explained in the same manner as the case of **C-EP1**, newly observed picosecond components (4-5 ps) most likely represent additional depolarization channels due to the excitation energy migration processes along the entire cyclic array.

In circularly arranged multichromophoric systems, the EEH times can be analyzed explicitly by simultaneous consideration of the two time constants, the annihilation time (τ_{ann}) and the depolarization time (τ_{dep}). Although neither exciton-exciton annihilation nor anisotropy depolarization directly represents the EEH times between the energy

hopping units, because they do not occur in a single donor-acceptor pair. The EEH times can be determined by synchronizing these two time constants by modeling the EEH mechanism.

4.7- Excitation energy hopping (EEH) processes in the macrorings. The description of the exciton-exciton annihilation and anisotropy depolarization has been well developed for the natural light-harvesting systems such as LH1 and LH2 that have macrocyclic arrangements with constant interchromophore interaction.[26] In these complexes, an explicit Förster-type incoherent EEH model has been described. Similarly, the EEH processes in **C-EP5** and **C-EP6** were analyzed using the S_1-S_1 exciton-exciton annihilation and anisotropy depolarization processes on the basis of Fleming's method.[26] Assuming migration-limited annihilation and a random-walk formalism of anisotropy decay, where the cofacial dimer unit can act as a coherent domain within the strong coupling limit, the EEH time can be obtained from the analytical depolarization and exciton-exciton annihilation times using Eqs. 1 and 2, where N is the number of excitation energy hopping sites (5 for **C-EP5** and 6 for **C-EP6**), α, the angle between the neighboring transition dipoles (108° for **C-EP5** and 120° for **C-EP6**), τ_{ann}, the slowest exciton-exciton annihilation time, τ_{dep}, the

depolarization time and $\tau_{hopping}$, the inverse of the nearest neighbor energy hopping rate:[26]

$$(1) \qquad \tau_{dep} = \frac{\tau_{hopping}}{4(1-\cos^2(2\pi/N))} = \frac{\tau_{hopping}}{4(1-\cos^2\alpha)}$$

$$(2) \qquad \tau_{ann} = \frac{N^2-1}{24}\tau_{hopping}$$

where τ_{dep} and τ_{ann} were obtained from, respectively, TAA and transient absorption decay depending on the pump power. For **C-EP5** where $N = 5$, we substituted $\tau_{dep} = 5.4$ ps in Eq. 1 and obtained $\tau_{hopping} = 19.5$ ps, and in a different approach, the substitution of $\tau_{ann} = 22$ ps in Eq. 2 gave $\tau_{hopping} = 22$ ps. Similarly, for **C-EP6** where $N = 6$, we substituted $\tau_{dep} = 4.2$ ps in Eq. 1 and obtained $\tau_{hopping} = 12.6$ ps for **C-EP6** and substituted $\tau_{ann} = 19$ ps in Eq. 2 and obtained $\tau_{hopping} = 13$ ps. Interestingly, the two different experimental observables, τ_{dep} and τ_{ann}, result in consistent EEH times ($\tau_{hopping}$) within small deviations. Thus, the excitation energy migration processes in these macrocyclic arrays can be well demonstrated by a Förster-type incoherent energy hopping model.

By taking an average value, the EEH times between the nearest neighboring coordination dimer units were determined to be 21 ± 1 ps for **C-EP5** and 12.8 ± 0.2 ps for **C-EP6**. In a previous study,[10] the same method has been applied to the EEH times for **C-P5** and **C-P6** to determine the EEH times of ~8.0 and ~5.3 ps, respectively. The difference in the EEH rates will be discussed in the next section.

4.8- Transition dipole coupling energy and EEH times in the macrorings.

As described in the previous section, the EEH times of larger ring systems (**C-EP5** and **C-EP6**) are longer than those of smaller ring systems (**C-P5** and **C-P6**), and considering the molecular size, the EEH times of pentagonal structures (**C-EP5** and **C-P5**) are longer than their corresponding hexagonal structures (**C-EP6** and **C-P6**).

The center-to-center distances between two adjacent slipped-cofacial dimers are 20.5 and 21 Å for **C-EP5** and **C-EP6**, respectively, which are larger than those of **C-P** series, 16.3 and 16.5 Å for **C-P5** and **C-P6**, respectively. The shorter EEH times of the smaller macrocycles, **C-P5** (~8.0 ps) and **C-P6** (~5.3 ps), suggest that the EEH time is dependent on the center-to-center distance between the coherent dimers. Naturally, one would expect that the larger distance between chromophores would lead to longer EEH times in cyclic array systems because both through-space and through-bond energy transfer rates strongly depend on the center-to-center distances proportional to R^{-6} and

$\exp^{-R}$, respectively. However, the shorter EEH times in hexagonal structures as compared to those in pentagonal structures are still questionable. This seems to stem from the fact that the angle 120° of the 1,3-bis(ethynyl)phenylene linker is better suited for hexagonal structures than it is for pentagonal ones. In this regard, the faster EEH times in hexagonal structures are thought to arise from the difference in the relative orientation between the nearest neighboring chromophores. As seen in the Förster-type energy transfer rate (Eq. 3) and the dipole coupling formula (Eq. 4), the orientation factor (κ) is in the numerator in both equations:

$$k_{TS} = \frac{8.8\times10^{-25}\kappa^2\Phi}{n^4R^6\tau}J \quad (3)$$

$$V_{ij} = \frac{5.04 f_L^2 \left|\vec{\mu}_i\right\|\vec{\mu}_j\left|\kappa\right.}{\varepsilon_{op}R_{TS}^3} \quad (4)$$

where n is the refractive index of the solvent, R, the center-to-center distance between donor and acceptor, τ, the fluorescence lifetime of an energy donor, κ, the orientation factor, Φ, the fluorescence quantum yield, J, the spectral overlap integral in Eq. 3, and V_{ij} is the transition dipole coupling energy, f_L, the Lorenz local field correction factor ($f_L = (\varepsilon_{op}+2)/3$), ε_{op}, the dielectric constant at optical frequencies, $\mu_{i,j}$, the transition dipole

moment, and R_{TS}, the center-to-center distance in nm, in which the subscript TS means through-space in Eq. 4.[27] The orientation factor κ is calculated by Eq. 5:

$$\kappa^2 = (\cos\theta_T - 3\cos\theta_i \cos\theta_j)^2 \quad (5)$$

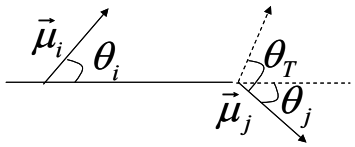

where θ_T is the dihedral angle between the two transition dipole moments, and θ_i and θ_j are the angles between these dipoles and the segment joining the two transition dipole moments. The angular parameters (θ_T, θ_i, and θ_j) values are 72°, 36°, and 36°, respectively, for **C-EP5**, and 60°, 30°, and 30°, respectively, for **C-EP6**. By substituting these values in Eq. 5 and assuming perfect planar pentagonal and hexagonal structures, κ is calculated to be 1.65 for **C-EP5** and 1.75 for **C-EP6**. The difference in κ seems small, but when the EEH processes occur from one hopping unit to the other one continuously, the effect of the small deviation in κ would increase exponentially. In summary, the larger value of κ in hexagonal structures induces a larger transition dipole coupling energy as compared to that in pentagonal structures, resulting in shorter EEH times in hexagonal structures. That is, well-oriented hexagonal arrays by the combinative conformation of chromophores and linkers exhibit faster EEH processes

than pentagonal arrays. Thus, the difference between the experimentally deduced EEH times of **C-EP5** and **C-EP6** is mainly accounted for by the orientation factor induced by the conformational differences. Indeed, the slightly more well-resolved Soret bands and red-shifted Q-bands of **C-EP6** as compared with those of **C-EP5** (Figure 4.4) support this arguments.

4.9- Assessment of antenna functions of the macrorings. The EEH time constants for **C-EP5** (21 ps) and for **C-EP6** (12.8 ps) are small enough compared with the lifetimes for **C-EP5** (1.42 ns) and **C-EP6** (1.38 ns). In addition to their fluorescence intensities, which are even larger than that of a monomeric unit, macrocyclic arrays are regarded as excellent LH antennae. Different EEH times between **C-EP5** and **C-EP6** indicate that EEH times depend strongly on the orientation factor of the constituent elements of macrocyclic arrays. However, the present study only investigated pentagonal and hexagonal macrocyclic arrays. The hypothesis should be confirmed for macrocycles larger than hexagonal arrays.

Comparison of the present EEH times with those of smaller macrocycles, **C-P5** (~8.0 ps) and **C-P6** (~5.3 ps), suggests that the EEH time is dependent on the center-to-center distance between the coherent coordination dimers. Coplanarity and electronic communication through the ethyne bond in **C-EP5** and **C-EP6** do not appreciably

accelerate the EEH times. Introduction of the ethyne moiety between porphyrin and phenylene causes the red-shifted absorption spectra of **C-EP5** and **C-EP6** compared to **C-P5** and **C-P6**. In addition, the Q(0,0) band of **C-EP5** and **C-EP6** increases considerably. These features are suitable as a second antenna into which excited energy flows from a peripheral higher energy antenna. Inspection of the overlap between the emission spectra of **C-P5** and **C-P6** and absorption spectra of **C-EP5** and **C-EP6** suggests that their composites provide an efficient energy cascade system like LH2 and LH1.

4.10- Experimental section for photophysical measurement

Steady-state absorption and fluorescence measurements. Steady-state absorption spectra were acquired with an UV-vis spectrometer (Shimadzu UV-3100PC and Scinco F4100). Steady-state fluorescence spectra of the samples were recorded on a fluorescence spectrometer (Hitachi F-4500 and Hitachi F2500) and corrected with the comparison of rhodamine B. Steady-state fluorescence excitation anisotropy spectra were obtained by changing the detection polarization on fluorescence path parallel or perpendicular to the polarization of the exciting light. Then anisotropy values were calculated as follows:

$$r = \frac{I_{VV} - GI_{VH}}{I_{VV} + 2GI_{VH}}$$

where I_{VV} (or I_{VH}) is the signal intensity when the excitation light is vertically polarized and only vertically (or horizontally) polarized portion of fluorescence is detected, denoting that the subscripts stand for excitation and detection polarization, respectively. The factor G is defined by I_{HV}/I_{HH} which is equal to the ratio of the sensitivities of the detection system for vertically and horizontally polarized light. All solvents with HPLC grade were purchased from Aldrich and used without further purification. All measurements were carried out at ambient temperature.

Time-resolved fluorescence decay measurements. Time-resolved fluorescence was detected using a time-correlated single-photon-counting (TCSPC) technique. As a excitation light source, a home-made cavity dumped Ti:sapphire oscillator was used which provides high repetition rate (200 ~ 400 kHz) of ultrashort pulses (100 fs at full width half maximum(FWHM)) pumped by a CW Nd-YVO_4 laser (Coherent, Verdi). The output pulse of the oscillator was frequency-doubled with a second harmonic crystal. The TCSPC detection system is consisted of multichannel plate photomultiplier (Hamamatsu, R3809U-51) with a cooler (Hamamatsu, C4878), a TAC (EG&G Ortec, 457), two discriminators (EG&G Ortec, 584 (signal) and Canberra, 2126 (trigger)), and two wideband amplifiers (Philip Scientific (signal) and Mini Circuit (trigger)). A personal computer with a multichannel analyzer (Canberra, PCA3) was used for data storage and processing. The overall instrumental response function was about 60 ps (fwhm). A sheet polarizer, set at an angle complementary to the magic angle (54.7°), was placed in the fluorescence collection system. The decays fitting analysis was performed by a deconvolution fitting program (LIFETIME) based on an iterative nonlinear least-squares deconvolution algorithm developed at the University of Pennsylvania.

Femtosecond transient absorption measurements. Dual-beam femtosecond time-resolved transient absorption spectrometer consisted of two independently-tunable home-made optical parametric amplifiers (OPA) pumped by a Ti:sapphire regenerative amplifier system (Spectra-Physics, Hurricane X) operating at 5 kHz repetition rate and an optical detection system. The OPA were based on non-collinearly phase-matching geometry and easily color-tuned by controlling delay between white light continuum pulses and pump pulses. The generated visible OPA pulses had a pulse width of ~35 fs and an average power of 10 mW at 5 kHz repetition rate in the range 500-700 nm. The probe beam was split into two parts. The one part of the probe beam was overlapped with the pump beam at the sample to monitor the transient (signal), while the other part of the probe beam was passed through the sample without overlapping the pump beam to compensate the fluctuation of probe beam (reference). The time delay between pump and probe beams was carefully controlled by making the pump beam travel along a variable optical delay (Newport, ILS250). To obtain the time-resolved transient absorption difference signal at specific wavelength, the monitoring wavelength was selected by using an interference filter. By chopping the pump pulses at 47 Hz, the modulated probe pulses as well as the reference pulses were detected by two separate photodiodes. The modulated signals of the probe pulses were measured by a

gated-integrator (SRS, SR250) and a lock-in amplifier (EG&G, DSP7265) and stored in a personal computer for further signal processing. The polarization angle between pump and probe beam was set to magic angle (54.7°) in order to prevent polarization-dependent signals.

Femtosecond transient absorption anisotropy measurements. For time-resolved anisotropy (TAA) measurement, both $I_{\parallel}$ and $I_{\perp}$ signals were collected simultaneously by combination of polarizing beam-splitter and dual lock-in amplifier. [28]

$$r(t) = (I_{\parallel} - I_{\perp}) / ((I_{\parallel} + 2I_{\perp})$$

where $I_{\parallel}$ and $I_{\perp}$ represent TA signals with the polarization of the pump and prove pulses being mutually parallel and perpendicular respectively. The polarization of pump pulse was set to vertical and that of probe pulse was set to 45° with respect to the pump pulse using Glan-laser polarizers and half-wave plates. The probe pulse after the sample cell was splitted by polarizing beam-splitter cube. Two photodiodes two BOXCAR averager and two lock-in amplifiers record the signal simultaneously in a single scan. As a standard anisotropy measurement, rhodamine 590 dye molecule in methanol was used, hiwhose rotational diffusion time was measured to 122 ps and the initial anisotropy r(0) value to 0.39, respectively, which are well-matched with other reference.[29] For all TA and TAA measurements, the absorption cell of 500 μm path length was used.

Chapter 5- Conclusion and Perspectives

Porphyrin-based supramolecular macrocyclic arrays were synthesized for the mimicry of photosynthetic light-harvesting (LH) antennae. Pentameric and hexameric macrocyclic porphyrin arrays **EP5** and **EP6** were constructed by complementary coordination of *m*-bis(ethynylene)phenylene-linked zinc(II) imidazolyl porphyrin **Zn-EP-Zn**. Porphyrin dimer units in the noncovalently linked **N-EP5** and **N-EP6** are conformationally flexible and undergo fast rotation around the ethyne axis on the NMR timescale. The shift behaviors of the phenylene protons in the ^{1}H NMR suggest that **N-EP5** and **N-EP6** adopt distinguishable macrocyclic architectures. These macrorings were covalently linked and identified as **C-EP5** (6832 Da) and **C-EP6** (8199 Da) by mass spectrometry. The molecular pentagon **C-EP5** and hexagon **C-EP6** were observed by high-resolution STM on gold surface. Each slipped-cofacial dimer part structurally defined by NMR was observed as one bright spot with the height of the dimer and assigned by comparison with the disassociated structure obtained at submolecular resolution. The electronic features of **C-EP5** and **C-EP6** have been characterized by steady-state and time-resolved photophysical measurements in pyridine and compared with various reference porphyrins. Introduction of the ethyne moiety induces a large transition dipole along the ethyne axis (B_x) and lowers the energy level of the Q(0,0)

band. Excitonic dipole-dipole coupling directed toward B_x was dominant, whereas that toward B_y was negligible. **C-EP5** and **C-EP6** did not show any sign of fluorescence quenching and their fluorescence quantum yields are larger than that of the constituent dimer **C-EP1**. This fluorescence property ensures that the macrorings of gable bisethynyl porphyrins represent a good model for the artificial light-harvesting complex. The energy hopping time constants through the coordination dimer units were determined by the analysis of anisotropy depolarization of the transient absorption spectra after polarized light excitation. At the same time, exciton-exciton annihilation rates were obtained from pump-power dependence on the transient absorption. The coincident time constants from two methods were 21 and 12.8 ps for **C-EP5** and **C-EP6**, respectively. Excitation energy hopping (EEH) times depend strongly on the orientation factor of the component transition dipoles in the macrocyclic arrays. The hexagonal macrocycle (**C-EP6**) afforded a faster EEH time compared to the pentagonal one (**C-EP5**), suggesting a better orientation factor of transition dipoles for hexagons, since similar tendency was also observed for the *m*-phenylene linked macrorings (**C-P5** and **C-P6**). This is a new finding for synthetic macrorings and should be useful in the design of efficient macrocyclic light-harvesting antennae.

Considering the fluorescence lifetime of 1.4 ns, rapid energy transfer should take place ~70-100 times in the macrorings during the excited state lifetime. These combined properties of **EP** macrorings prove the excellent light-harvesting antenna models of the LH2-B850 type not only in their structure, but also in their function.

Future work will focus on incorporation of these LH2-type **EP** macrorings into elaborate photosynthetic model system. For such a system, an LH1-type antenna model is required. Recently, the author's group has succeeded in the construction of an LH1-type light-harvesting complex by specific trimerization of Zn(II) imidazolyl trisporphyrin.[8b] This design concept along with the new findings in this work will be employed to construct larger macrorings of porphyrin trimer that have more acetylene moieties and can accommodate energy accepting units in their cavities. These LH1-type antenna rings are expected to absorb in the red and thus, can accept the singlet excitation energy from **EP** rings and transfer the excitation to a reaction center (RC)-type acceptor. The composites of these LH1-(RC) and LH2-type macrorings should provide a sound basis for the further study of energy transfer among chromophores which spatial energetic-arrangement mimics the photosynthetic unit arrangement in purple bacteria.

References and Notes

(1) (a) van Grondelle, R. *Biochim. Biophys. Acta* **1985**, *811*, 147. (b) Pullerits, T.; Sundström, V. *Acc. Chem. Res.* **1996**, *29*, 381.

(2) (a) Sundström, V.; Pullerits, T.; van Grondelle, R. *J. Phys. Chem. B* **1999**, *103*, 2327. (b) van Grondelle, R.; Dekker, J. P.; Gillbro, T.; Sundström, V. *Biochim. Biophys. Acta* **1994**, *1187*, 1-65.

(3) (a) McDermott, G.; Prince, S. M.; Freer, A. A.; Hawthornthwaite-Lawless, A. M.; Papiz, M. Z.; Cogdell, R. J.; Isaacs, N. W. *Nature* **1995**, *374*, 517. (b) Koepke, J.; Hu, X.; Muenke, C.; Schulten, K.; Michel, H. *Structure* **1996**, *4*, 581. (c) Karrasch, S.; Bullough, P. A.; Ghosh, R. *EMBO J.* **1995**, *14*, 631. (d) Hu, X.; Damjanovic, A.; Ritz, R.; Schulten, K. *Proc. Natl. Acad. Sci. U.S.A.* **1998**, *95*, 5935.

(4) (a) Harvey, P. D. In *The Porphyrin Handbook*; Kadish, K. M., Smith, K. M., Guilard, R., Eds.; Academic Press: New York, 2003; Vol. 18, pp 63-250. (b) Kim, D.; Osuka, A. *Acc. Chem. Res.* **2004**, *37*, 735. (c) Holten, D.; Bocian, D. F.; Lindsey, J. S. *Acc. Chem. Res.* **2002**, *35*, 57-69. (d) Choi, M.-S.; Yamazaki, T.; Yamazaki, I.; Aida, T. *Angew. Chem., Int. Ed.* **2004**, *43*, 150 –158. (e) Imahori, H. *J. Phys. Chem. B* **2004**, *108,* 6130-6143. (f) Satake, A.; Kobuke, Y. *Tetrahedron*, **2005**, *61*, 13–41. (g) Balaban, T. S. *Acc. Chem. Res.* **2005**, *38*, 612-623. (h) You, C.-C.; Dobrawa, R.; Saha-Möller, C. R.; Würthner, F. *Top. Curr. Chem.,* **2005**, *258*, 39.

(5) Gust, D.; Moore, T. A.; Moore, A.L. *Acc. Chem. Res.* **2001**, *34*, 40.

(6) (a) Lehn, J.-M. *Science* **2002**, *295*, 2400. (b) Ogawa, K.; Kobuke, Y. *Angew. Chem., Int. Ed.* **2000**, *39*, 4070. (c) Hwang, I.-W.; Kamada, T.; Ahn, T. K.; Ko, D. M.; Nakamura, T.; Tsuda, A.; Osuka, A.; Kim, D. *J. Am. Chem. Soc.* **2004**, *126*, 16187.

(7) (a) Shi, X.; Barkigia, K. M.; Fajer, J.; Drain, C. M. *J. Org. Chem.* **2001**, *66*, 6513-6522. (b) Haycock, R. A.; Hunter, C. A.; James, D. A.; Michelsen, U.; Sutton, L. R. *Org. Lett.* **2000**, *2*, 2435-2438.

(8) (a) Takahashi, R.; Kobuke, Y. *J. Am. Chem. Soc.* **2003**, *125*, 2372-2373. (b) Kuramochi, Y.; Satake, A.; Kobuke, Y. *J. Am. Chem. Soc.* **2004**, *126*, 8668-8669. (c) Shoji, O.; Okada, S.; Satake, A.; Kobuke, Y. *J. Am. Chem. Soc.* **2005**, *127,* 2201-2210. (d) Hajjaj, F.; Yoon, Z. S.; Yoon, M.; Park, J.; Satake, A.; Kim, D.; Kobuke, Y. *J. Am. Chem. Soc.* **2006**, *128,* 4612. (e) Ikeda, C.; Satake, A.; Kobuke,

Y. *Org. Lett.* **2003**, *5*, 4935-4938. (f) Takahashi, R.; Kobuke, Y. *J. Org. Chem.* **2005**, *70*, 2745-2753.

(9) (a) Kobuke, Y. *Struct Bond.* **2006**, *121*, 49-104. (b) Wakao, N.; Yokoi, N.; Isoyama, N.; Hiraishi, A.; Shimada, K.; Kobayashi, M.; Kise, H.; Iwaki, M.; Ithoh, S.; Takaichi, S.; Sakurai, Y. *Plant Cell Physiol.* **1996**, *37*, 889.

(10) Kim, D.; Miyasaka, H.; Kobuke, Y.; et al. *Chem. Eur. J.* **2005**, *11*, 3753.

(11) (a) Ferran, A. V.; Watson, Z. C.; Bampos, N.; Sanders, J. K. *J. Org. Chem.* **1997**, *62*, 240-241. (b) Tomizaki, K.-Y.; Yu, L.; Wei, L.; Bocian, D. F.; Lindsey, J. S. *J. Org. Chem.* **2003**, *68*, 8199-8207. (c) Rucareanu, S.; Schuwey, A.; Gossauer, A. *J. Am. Chem. Soc.* **2006**, *128,* 3396.

(12) Sonogashira, K.; Tohda, Y.; Hagihara, N. *Tetrahedron Lett.* **1975**, *16*, 4467-4470.

(13) Ogawa, K.; Ohashi, A.; Kobuke, Y. *J. Am. Chem. Soc.* **2003**, *125*, 13356.

(14) (a) Chi, X.; Guerin, A. J.; Haycock, R. A.; Hunter, C. A.; Sarson, L. D. *J. Chem. Soc., Chem. Commun.* **1995**, 2563. (b) Ercolani, G. *J. Phys. Chem. B* **1998**, *102,* 5699.

(15) The covalently linked macrorings tend to aggregate in common organic solvents which hampered their characterization by NMR. **C-EP5** and a mixture of **C-EP5** and **C-EP6** are partially soluble in $CHCl_3$. Pyridine is the only solvent in which the covalently linked rings showed a remarkable solubility, therefore, it was employed in the photophysical characterizations but not in the STM measurements due to its high boiling point.

(16) Ohashi, A.; Satake, A.; Kobuke, Y. *Bull. Chem. Soc. Jpn.* **2004**, *77*, 365-374.

(17) Shoji, O.; Tanaka, H.; Kawai, T.; Kobuke, Y. *J. Am. Chem. Soc.* **2005**, *127*, 8598.

(18) On the basis of mass analysis in Figure 3.1 (a).

(19) (a) Tanaka, H.; Kawai, T. *J. Vac. Sci. Technol. B* **1997**, *15*, 602. (b) Tanaka, H.; Kawai, T. *Surf. Sci.* **2003**, *539*, L531.

(20) Satake, A.; Tanaka, H.; Hajjaj, F.; Kawai, T. Kobuke, Y. *Chem. Commun.* **2006**, *24*, 2542-2544.

(21) (a) Nakano, A.; Yasuda, Y.; Yamazaki, T.; Akimoto, S.; Yamazaki, I.; Miyasaka, H.; Itaya, A.; Murakami, M.; Osuka, A. *J. Phys. Chem. A* **2001**, *105*, 4822-4833. (b) Hindin, E.; Kirmaier, C.; Diers, J. R.; Tomizaki, K.-Y.; Taniguchi, M.; Lindsey, J. S.; Bocian, D. F.; Holten, D. *J. Phys. Chem. B* **2004**, *108*, 8190-8200.

(22) Seybold, P. G.; Gouterman, M. *J. Mol .Spectrosc.* **1969**, *31*, 1.

(23) Kasha, M. *Radiat .Res.* **1963**, *20*, 55-70.

(24) Hwang, I.-W.; Ko, D. M.; Ahn, T. K.; Yoon, Z. S.; Kim, D.; Peng, X.; Aratani, N.; Osuka, A. *J. Phys. Chem. B* **2005**, *109*, 8643-8651.

(25) Osuka, A.; Kim, D.; et al. *J. Phys. Chem. B* **2005**, *109*, 11223-11230.

(26) Bradforth, S. E.; Jimenez, R.; van Mourik, F.; van Grondelle, R.; Fleming, G. R. *J. Phys. Chem.* **1995**, *99*, 16179-16191.

(27) Morandeira, A.; Vauthey, E.; Schuwey, A.; Gossauer, A. *J. Phys. Chem. A* **2004**, *108*, 5741-5751.

(28) Min, C.-K.; Joo, T.; Yoon, M.-C.; Kim, C. M.; Hwang, Y. N.; Kim, D.; Aratani, N.; Yoshida, N.; Osuka, A. *J. Chem. Phys.* **2001**, *114*, 6750.

(29) Philips, L. A.; Webb, S. P.; Yeh, S. W.; Clark, J. H. *J. Phys. Chem.* **1985**, *89*, 17.

Acknowledgement

I am deeply indebted to my advisor Prof. Yoshiaki Kobuke for entrusting me with this interesting project and teaching me to be the researcher I have grown to become, while working with him. He has always been a source of inspiration as a scientist and I sincerely appreciate his patience and understanding in spite of my faults as a fledgling experimental chemist. I am glad I had him as an advisor and will owe him a debt of gratitude for a long time.

I am eternally grateful to Associate Prof. Shin-ichi Kugimiya, Dr. Akiharu Satake and Dr. Kazuya Ogawa for all that they taught me about supramolecular chemistry. Without their assistance and instructions, this work would not have been possible. I always had the good fortune of being in the same group with Dr. Akiharu Satake, who was always able to spend time to discuss with me various issues regarding chemistry and life in general. My work under his instructions has been immensely rewarding. It would be more than fair to say that he has been one of those people who helped me along the way and I wish him all the best in his career.

I truly appreciate my defense committee members, Prof. M. Kataoka, Prof. K. Kakiuchi and Prof. M. Aihara, for their interest in my work and constructive critique. Their feedback, advice and suggestions are highly appreciated.

I would like to express my gratitude to our collaborators; Prof. Dongho Kim and his members at Yonsei University/Korea for the detailed photophysical investigation (Chapter 4), Prof. Tomoji Kawai and his group of Osaka University for the STM measurements (Chapter 3, section 3.3).

I am indebted to the Japanese Ministry of Education, Culture, Sports, Science and Technology (Monbukagakusho) for granting me the scholarship and generous stipend that made this research possible. I also wish to thank Inoue Foundation for Science for the financial support that allowed me to participate in PACIFICHEM 2005/USA.

I am also indebted to my amazing colleagues and friends at NAIST who made life beyond work so much fun and meaningful at the same time. Without their support and affection, I could not have endured the difficult phases in a graduate student's stressful life! Those long nights working on synthesis and the great times at Osaka-USJ, Nagashima, Disneyland, F1 racing and Hawaii will not be forgotten!!

Finally, I would like to thank my family for their unceasing support as I set off around the world on yet another adventure.

FATIN HAJJAJ

NAIST, 2006

List of Publications and Presentations

学位論文の主たる部分を公表した論文

“Assemblies of Supramolecular Porphyrin Dimers in Pentagonal and Hexagonal Arrays Exhibiting Light-Harvesting Antenna Function”
Fatin Hajjaj, Zin Seok Yoon, Min-Chul Yoon, Jaehong Park, Akiharu Satake, Dongho Kim, and Yoshiaki Kobuke
Journal of the American Chemical Society, 2006, 128, 4612–4623

“Single Molecular Observation of Penta- and Hexagonic Assembly of Bisporphyrin on a Gold Surface”
Akiharu Satake, Hiroyuki Tanaka, Fatin Hajjaj, Tomoji Kawai and Yoshiaki Kobuke
Chemical Communications, 2006, 24, 2542-2544

【国際学会発表】
(口頭招待発表)
“Supramolecular Antenna Arrangements of Porphyrins and Their Photophysical Properties”
○Yoshiaki Kobuke, Yusuke Kuramochi, Fatin Hajjaj, and Akiharu Satake
6th International Conference on Tetrapyrrole Photoreceptors in Photosynthetic Organisms, Luzern, Switzerland, Septmber, 2005

（ポスター）
“Self-Assembled Macrorings of 1,3-Bisethynephenylene-Linked Porphyrin as Mimics of Photosynthetic Light-Harvesting Complexes”
○Fatin Hajjaj, Akiharu Satake, Zin Seok Yoon, Min-Chul Yoon, Jaehong Park, Dongho Kim, and Yoshiaki Kobuke
The 2005 NAIST/GIST Joint Symposium on Advanced Materials, Gyoungju, Korea, November 2005

“Self-Assembled Hexameric and Pentameric Macrorings of 1,3-Bis(ethynyl)phenylene-Linked Porphyrin”
○Fatin Hajjaj, Akiharu Satake, and Yoshiaki Kobuke
The 2005 International Chemical Congress of Pacific Basin Societies (PACIFICHEM 2005), Hawaii, USA, December 2005 (**Poster Award**).

【国内学会発表】

（口頭発表）

“Construction of Supramolecular Rings of 1,3-Bis(ethynyl)phenylene-Linked Bis(imidazolylporphyrin)”

○Hajjaj, Fatin; Satake, Akiharu; Kobuke, Yoshiaki

日本化学会第 85 回春季年会、神奈川大学、2005 年 3 月

（口頭発表）

“Self-Assembled Hexameric and Pentameric Macrorings as a Light-Harvesting Antenna Mimic”

○Hajjaj, Fatin; Satake, Akiharu; Kobuke, Yoshiaki; Tanaka, Hiroyuki; Kawai, Tomoji

The 20th Symposium on Biofunctional Chemistry, Nagoya City University, September 2005

（ポスター発表）

「超分子ポルフィリンリングの可視化 」

○佐竹彰治・荘司長三・ハジャジ ファティン・小夫家芳明・田中裕行・川合知二

CREST「分子複合系の構築と機能」公開シンポジウム、東京、2005 年 10 月

（口頭発表）

“Structural Analysis of Supramolecular Porphyrin Macrocycles in Solution and on Gold Surface”

○Satake, Akiharu; Hajjaj, Fatin; Kobuke, Yoshiaki; Tanaka, Hiroyuki; Kawai, Tomoji

日本化学会第 86 回春季年会、日本大学、2006 年 3 月

（口頭発表）

“Assessment of Light-Harvesting Antenna Function for Pentagonal and Hexagonal Macrorings of Acetylene-Linked Zn(II) Gable Porphyrin”

○Hajjaj, Fatin; Satake, Akiharu; Kobuke, Yoshiaki; Yoon, Zin Seok; Kim, Dongho

日本化学会第 86 回春季年会、日本大学、2006 年 3 月